LEARNING THE HAMILTONIAN OF DISORDERED MATERIALS WITH EQUIVARIANT GRAPH NETWORKS

Anonymous authors
Paper under double-blind review

ABSTRACT

Graph neural networks (GNNs) have shown promise in learning the ground-state electronic properties of molecules and crystalline materials, subverting computationally intensive density functional theory (DFT) calculations. Materials with structural disorder, however, are more challenging to learn as they exhibit higher complexity and a more extensive palette of local atomic environments, all of which require large (10+ Å) cells to be accurately captured. In this work, we adapt efficient equivariant GNN approaches to learn disordered materials' electronic properties, represented by the Hamiltonian matrix ($\boldsymbol{H}$). Since creating a large graph corresponding to the whole structure of interest would be computationally prohibitive, we introduce an *augmented partitioning* approach in which the graph is sliced into multiple partitions, each augmented with masked virtual nodes and edges. This method maintains correct atomic neighborhoods within a single message passing layer, allowing for the network to learn the electronic properties of amorphous HfO_2 materials with 3,000 nodes (atoms), 500,000+ edges, and $\sim$28 million orbital interactions (non-zero entries of $\boldsymbol{H}$).

1 INTRODUCTION

Predicting structure-property relationships in atomically resolved materials lends itself optimally to graph-structured data. Graph Neural Networks (GNNs) have proven capable of learning these relationships while constrained by their underlying symmetries (Veličković et al. (2018)). Trained networks have been able to learn molecular- and atomic-level quantities (Wang et al. (2023)), circumventing otherwise computationally prohibitive simulations at the *ab initio* level. More recently, GNNs have been adapted to predict electronic properties, described by a discretized ground-state Hamiltonian matrix $\boldsymbol{H}$. Rapid and accurate constructions of $\boldsymbol{H}$ can unlock *in silico* explorations of the large design space of electronic materials (Klinkert et al. (2020)).

The matrix $\boldsymbol{H}$ can be decomposed into sub-matrices $\boldsymbol{H}_{i,j}$ that encode the coupling between the sets of atomic orbitals located on atoms i and j. These coupling terms are a function of the identity and relative coordinates of the local environment. Predicting such electronically resolved information introduces additional challenges over atomically resolved quantities, as the output data is equivariant under rotation. Existing work on electronic property prediction has mainly treated the cases of small molecules (Zhong et al. (2023); Yu et al. (2023b); Bai et al. (2021)) and well-ordered materials (Li et al. (2022); Gong et al. (2023); Wang et al. (2024a)). The graph representations of these structures are fairly small - small molecules contain only a few atoms, and in crystalline materials all relevant structural information can be captured within the smallest repeating unit cell.

Many applications, however, require the computation of the electronic properties of materials with structural disorder, such as local or extended defects, or in an amorphous phase (Ducry et al. (2020); Kaniselvan et al. (2023); Strand et al. (2018)). These materials typically contain a limited number of atomic species, from 2 to 5, with quasi-random distributions. Accurate *ab initio* simulations of the resulting disordered atomic structures are only possible if large unit cells composed of hundreds to thousands of atoms are used (Repa & Fredin (2023)). As a consequence, prohibitively expensive computations must be performed with a density functional theory (DFT) tool to obtain their electronic properties. The prospect of applying deep-learning solutions to handle such materials is thus particularly attractive. To be of practical relevance, however, they should be able to generalize to large scales.

Here, we extend equivariant GNN approaches to learn and predict the electronic properties of materials in amorphous phases by fitting the sub-blocks of the ground-state Hamiltonian $\boldsymbol{H}$ in matrix form. Our main contributions are:

- We develop an efficient GNN-based model for electronic property prediction, by combining (1) the SO(2)-convolution approach detailed in Passaro & Zitnick (2023), (2) the equivariant attention mechanism introduced in Liao et al. (2023), and (3) concepts from Gong et al. (2023) and Wang et al. (2024a) to introduce learnable node/edge embeddings along with basis transformation layer to pre-process the targets and map predictions to the Hamiltonian output. We provide the code for this implementation in [the Supporting Materials].
- As the graphs required to capture amorphous disorder are necessarily large and incur high memory consumption in a full-batch training environment, we propose an efficient *augmented partitioning* method that partitions the input graphs and corrects atomic environments with masked virtual nodes and edges. Our method allows for arbitrarily large graphs to be broken down into partitions that can fit into GPU memory during training, without compromising the achievable testing accuracy.

We combine our model and *augmented partitioning* approach to treat a real example with practical scientific relevance. Specifically, we consider hafnium dioxide (HfO_2), one of the most technologically relevant amorphous oxides (Choi et al. (2011)). The theoretical study of defects and transport properties in HfO_2 is relevant to several research areas, from optimizing gate dielectrics for transistors (Strand et al. (2018)) to developing new resistive-switching technologies enabling in-memory computing (Kaniselvan et al. (2023)). With this, we achieve a prediction accuracy of 5.87 meV, matching the eigenvalues of $\boldsymbol{H}$ to within 0.87% relative L1 error, on structures with 3,000 atoms, which require several (3.65) hours to compute using DFT. Our work advances applications of equivariant GNNs towards practical use cases in computational physics, chemistry, and materials science.

2 Background & Related Work

The electronic properties of a material refer to its set of energy levels (ε) and wavefunctions (ψ) that electrons can occupy. They correspond to the eigenvalues and eigenvectors of the Hamiltonian matrix $\boldsymbol{H}$ describing the atomic system of interest. This quantity is a function of the location (relative positions $\{\boldsymbol{r}_i\}$) and identity (atomic numbers $\{Z_i\}$) of all constituent atoms $\{i\}$ (Hohenberg & Kohn (1964)). Therefore, predicting the electronic properties consists of learning the mapping $F : \{\boldsymbol{r}_i, Z_i\} \rightarrow \boldsymbol{H}$ between the atomic structure and the elements of the corresponding Hamiltonian matrix (**Fig. 1**).

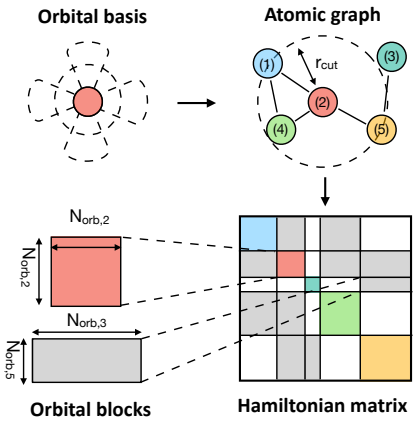

Figure 1: Schematic of the mapping between the atomic graph and the blocks of the Hamiltonian matrix $\boldsymbol{H}$ in the localized orbital basis of choice. Each orbital block represents the couplings between atomic orbitals on the same atom ($\boldsymbol{H}_{i,i}$, diagonal) or between two different atoms within r_{cut} ($\boldsymbol{H}_{i,j}$, off-diagonal).

The entries of the ground-state Hamiltonian matrix $\boldsymbol{H}$ are typically computed from first-principles with DFT (Kohn & Sham (1965)). In several widely used codes, the wavefunctions are expanded into a basis $|\varphi\rangle$ of non-orthogonal atomic orbitals localized around atomic positions, each built, for example, from contracted Gaussian functions (Kühne et al. (2020); Neese (2011)). These orbitals transform like spherical harmonics under rotation $\hat{\boldsymbol{r}} \rightarrow \hat{\boldsymbol{r}}'$: $Y^l_m(\hat{\boldsymbol{r}}') = \sum_{m'} \boldsymbol{D}^l_{mm'}(\boldsymbol{R}) Y^l_{m'}(\hat{\boldsymbol{r}})$. Here, Y^l_m is the spherical harmonic of degree l and order $m \in \{-l, \dots, l\}$. $\boldsymbol{D}^l_{mm'}(\boldsymbol{R})$ is the Wigner-D matrix of degree l corresponding to the rotation $\boldsymbol{R}$, which transforms the corresponding spherical harmonic. $\hat{\boldsymbol{r}}$ and $\hat{\boldsymbol{r}}'$ are normalized direction vectors.

The localized nature of the basis states leads to finite spatial overlaps between them. The resulting Schrödinger equation at the core of DFT takes the form of a generalized eigenvalue problem: $\boldsymbol{H}\psi = \varepsilon \boldsymbol{S}\psi$. Here, the Hamiltonian matrix $\boldsymbol{H}^{(N\times N)}$ has entries $\boldsymbol{H}_{i,j} = \langle \varphi_i | \hat{H}(\boldsymbol{r}) | \varphi_j \rangle$ where $\hat{H}(\boldsymbol{r})$ is the so-called Hamiltonian operator, while the Overlap matrix $\boldsymbol{S}^{(N\times N)}$ is made of $\boldsymbol{S}_{i,j} = \langle \varphi_i | \varphi_j \rangle$. They are both coarse-grained matrices of size $N = \sum_k N^k_{atoms} \cdot N^k_{orb}$, where N_{atoms} is the number

of atoms, N_{orb} the number of orbitals per atom, and k indexes over the different atomic species found in the system. Note that $\boldsymbol{S}$ reduces to the identity matrix in case of an orthogonal basis $|\varphi\rangle$. Otherwise, it can be directly computed from the basis as the problem's physics does not influence it.

The Hamiltonian matrix can be decomposed into sub-matrices $\boldsymbol{H}_{i,j}$ of size $(N^i_{orb} \times N^j_{orb})$, each describing the interactions between all basis elements (orbitals) on atoms i and j. Diagonal blocks ($\boldsymbol{H}_{i,i}$) are the interactions between orbitals on the same atom. When represented on a local basis, the matrix is near-sighted; the interactions between orbitals on different atoms decay exponentially with increasing interatomic distance. Since an atomic orbital basis is used, the sub-matrices are equivariant under rotation of the atomic bonds, with their transformation properties related by the Wigner-D matrix.

2.1 Challenges unique to disordered materials

Computing the electronic properties of disordered materials with DFT still requires defining a repeating 'unit cell' and using periodic boundaries to avoid dangling bonds. This periodicity, however, can alter the material's amorphous nature if the repeating unit cell is too small. Atoms can interact with all their periodic images, leading to non-physical phenomena such as the formation of coherent electronic states across cells. These phenomena can be prevented by constructing 'large-enough' unit cells (12+ Å (Repa & Fredin (2023)) to a few nanometers (Ducry et al. (2020))) that better approximate disorder. Generating the Hamiltonian matrix $\boldsymbol{H}$ of these systems with DFT involves tens to hundreds of self-consistent field (SCF) loops, each requiring the diagonalization of an intermediate $\boldsymbol{H}$. As this numerical operation scales with $\mathcal{O}(N^3_{atoms})$, analyzing electronic properties for large amorphous systems (or different amorphous representations of the same material) is very often computationally unaffordable.

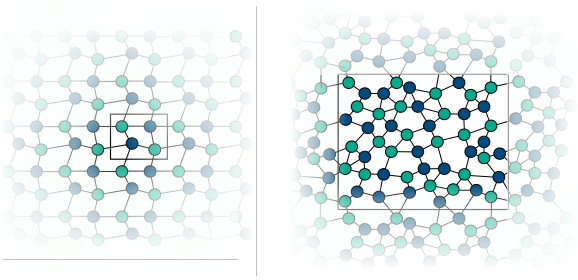

Figure 2: Illustration of the difference between ordered (left) and disordered materials (right), whose structural features can only be captured by defining a large unit cell. In both cases, the smallest repeating unit cell is delimited by a black box, while the circles/lines correspond to atoms/bonds.

2.2 Development of models for the prediction of electronic properties

Only a few studies have attempted to directly predict the Hamiltonian matrix $\boldsymbol{H}$ rather than directly fitting invariant quantities such as the total energy. The key is to constrain the solution space by leveraging prior knowledge of physical symmetries, e.g., rotational equivariance of orbital blocks.

Several works leverage local structure descriptors containing sufficient detail about each atom's environment. The mapping between these descriptors and the orbital blocks of the Hamiltonian was then learned through Kernel Ridge Regression (Hegde & Bowen (2017)) or multilayer neural networks (Schütt et al. (2019); Gu et al. (2024)). Certain descriptors, such as Atomic Cluster Expansion (ACE) (Drautz (2020)), can be extended to orbitally resolved data (Nigam et al. (2022)) and used to predict the Hamiltonian matrix of crystalline materials (Zhang et al. (2022)). These approaches achieved prediction accuracy of a few meV on small-molecule datasets. Rotational equivariance was enforced through the descriptors (Zhang et al. (2022)) or data augmentation (Schütt et al. (2019)). Initial GNN-based approaches, such as the network developed by Li et al. (2022), are intrinsically invariant to the translation and permutation of the inputs. Information about the rotational equivariance was incorporated by rotating to a pre-selected axis before training, which reduces the problem to a rotationally invariant one.

In equivariant GNNs, the predicted Hamiltonian rotates along with the input (Yu et al. (2023b); Zhang et al. (2024); Batatia et al. (2023); Gong et al. (2023)), which requires maintaining SO(3)-equivariance within the model. This means that all network operations f acting on input embedding x^l of degree l must satisfy: $f(\boldsymbol{D}^l(\boldsymbol{R}) \cdot \boldsymbol{x}^l) = \boldsymbol{D}^l(\boldsymbol{R}) \cdot f(\boldsymbol{x}^l)$. The networks are trained using Message Passing (MP), where each MP layer works as follows: An atom i receives input messages from each neighboring source atom j. Each input message goes through convolution operations

that combine features with different l while preserving equivariance; a specific output embedding $\boldsymbol{x}_{ji}^{l_3}$ of degree l_3 can be computed through: $\boldsymbol{x}_{ji}^{l_3} = \sum_{l_1,l_2} \boldsymbol{x}_j^{l_1} \otimes_{l_1,l_2}^{l_3} h_{l_1,l_2,l_3} Y^{l_2}(\hat{\boldsymbol{r}}_{ji})$. Here, $\hat{\boldsymbol{r}}_{ji}$ is a normalized vector indicating the direction of the edge connecting the atoms j and i, and h is a set of trainable weights. The sum runs over tensor products which take $\boldsymbol{x}_j$ (a source input embedding of degree l_1) and Y^{l_2} (a filter spherical harmonic embedding of degree l_2) and produce the output embedding:

$$(\boldsymbol{x}_j^{l_1} \otimes_{l_1,l_2}^{l_3} Y^{l_2}(\hat{\boldsymbol{r}}_{ji}))_{m_3}^{l_3} = \sum_{m_1,m_2} (\boldsymbol{x}_j^{l_1})_{m_1} C_{(l_1,m_1),(l_2,m_2)}^{l_3,m_3} h_{l_1,l_2,l_3} Y_{m_2}^{l_2}(\hat{\boldsymbol{r}}_{ji}),$$

where the $C_{(l_1,m_1),(l_2,m_2)}^{l_3,m_3}$ are the Clebsch-Gordan coefficients that are indexed by the order m and degree l of the input, filter, and output embeddings. The combination of feature (x) and geometric ($\hat{r}$) information along each edge encodes both the identity and structure of the system. These 'Tensor Field Networks' (TFNs) (Thomas et al. (2018)) achieve state-of-the-art accuracy on small molecule (Yu et al. (2023b)) and crystalline (Gong et al. (2023)) datasets. However, they are also much more computationally expensive. The network training scales with $\mathcal{O}(l_{max}^6)$, where l_{max} is the maximum degree of the angular momentum considered. Fully, E(3)-equivariant networks are difficult to apply beyond a few atoms (Zhang et al. (2024)).

Recently, the computational cost of training equivariant GNNs has been significantly reduced by combining the benefits of data rotation and equivariant network operations. These approaches take advantage of the fact that when edges are rotated to align with a fixed axis (y or z depending on convention), the only non-zero spherical harmonic components are those of order m = 0. By keeping track of the bond vectors and performing internal spherical rotations, complex SO(3) convolutions can thus be reduced into SO(2) linear convolution operations (Passaro & Zitnick (2023)). Additionally, under these conditions, the Clebsch-Gordan coefficients exhibit a predictable sparsity pattern (non-zero only when $m_3 = \pm m_1$). Altogether, the scaling reduces to $\mathcal{O}(l_{max}^3)$ (Wang et al. (2024a)), and the network's training speeds up, enabling the use of higher-order angular momenta (l_{max}) and more parameters to capture finer, more complex details of the surrounding environment. An advanced SO(2) convolution network was developed by Passaro & Zitnick (2023) (eSCN)) and further expanded by Liao et al. (2023) (EquiformerV2) with the inclusion of equivariant attention and separable activation layers. A subsequent implementation of this approach on Hamiltonians by Wang et al. (2024a) achieved better performance on custom crystalline 2D-material datasets compared to previous tensor field and invariant networks.

3 METHODS

We adapt the 'EquiformerV2' network by incorporating concepts from Gong et al. (2023) and Wang et al. (2024a). In this section, we present an overview of the methods used to initialize the graph, construct the network, and propose an efficient *augmented partitioning* approach to train it. Relevant implementation details and ablation studies are presented in **Section 4** and **Appendices A, C, D**.

3.1 NETWORK LAYOUT

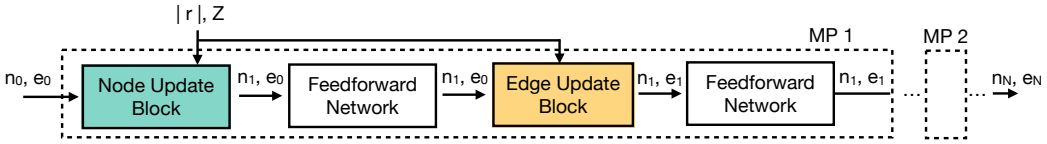

Figure 3: High-level overview of the network, illustrating the update of node features ($\boldsymbol{n}_X$) and edge features ($\boldsymbol{e}_X$) after message passing layer X (MP X). Z refers to atomic numbers, while r_{ij} is the set of scalar distances between atoms.

When constructing a given material's graph, we can leverage the Hamiltonian's near-sightedness to only retain edges corresponding to atoms within a fixed interaction distance r_{cut}, beyond which the interactions are negligible. Orbitals located on different atoms can interact with each other over distances of ∼10 Å, giving rise to specific off-diagonal blocks in the Hamiltonian matrix.

The graph's nodes/edges are initialized with an embedding of shape $(N_n,\ (l_{max}+1)^2,\ d_{sphere,n})$/$(N_e,\ (l_{max}+1)^2,\ d_{sphere,e})$, where $N_{n/e}$ is the number of nodes/edges, $d_{sphere,n/e}$ the channel dimension for embeddings, and l_{max} the maximum degree of the features. The $l=0$ channels of the node embeddings are initialized with atomic numbers, while the $l=0$ of the edge embeddings are initialized with the scalar distance between the two connecting nodes, expanded in the chosen basis, here Gaussian functions. All other components are initially set to 0. The orbital blocks representing the interaction between atoms are flattened into 1D tensors to form the labels for each node/edge during the supervised training process. They are then converted from uncoupled to coupled basis using a Wigner-Eckart transformation (**Appendix A.1**).

During training, each MP layer updates the node, and then the edge representations. Within the node update block, each node i receives messages from each of its neighbors j, consisting of the concatenated embeddings $\boldsymbol{n}_i$, $\boldsymbol{n}_j$, and that of the edge $\boldsymbol{e}_{ji}$, rotated to align with the z-axis. After SO(2) convolutions are performed on the input messages, the resulting output messages are rotated back to their original orientations and aggregated onto the node i to update its embedding $\boldsymbol{n}_i$. The updated node embeddings are then used to update the edges through a similar process, without the attention layer. Subsequently, the node embeddings in the next message-passing layer are updated with the new edge embeddings. A high-level overview of the network is presented in **Fig. 3**, and a more detailed outline can be found in **Appendix A**. During the inference phase, the output is converted back to the uncoupled basis through a Wigner-Eckart layer (**Appendix A.1**) to reconstruct the Hamiltonian matrix $\mathbf{H}$.

Our network architecture is similar to that of EquiformerV2 and DeepH2. A particular difference lies in the use of gate activation layers instead of the S^2 activation layer of EquiformerV2. Although the S^2 layer allows for non-linearity to be introduced to higher-order features, achieving numerically perfect equivariance requires a large grid size, making it computationally expensive when implemented on large graphs (Passaro & Zitnick (2023)).

3.2 Augmented partitioning with masked virtual nodes/edges

Training GNN representations of the large amorphous materials considered here incurs high memory consumption and long computation times per epoch (**Appendix G.2**). The dense connectivity of these graphs also leads to heavy communication overhead in full-batch distributed approaches (Wan et al. (2022)).

A variety of methods have been developed to reduce the memory requirements and increase the amount of parallelism during training of large graphs (Besta & Hoefler (2024)). However, they do not cover the specificity of our application. Much of previous work is concerned with modifying connectivity to effectively propagate long-range information, for example, by dividing the graph into sub-graphs and passing messages intra- and inter-subgraph (Liao et al. (2018)), or introducing virtual nodes to transfer messages over longer distances (Qian et al. (2024)). Such approaches are unnecessary in our case since the graph is nearsighted and long-range interactions are negligible (**Appendix F.1**).

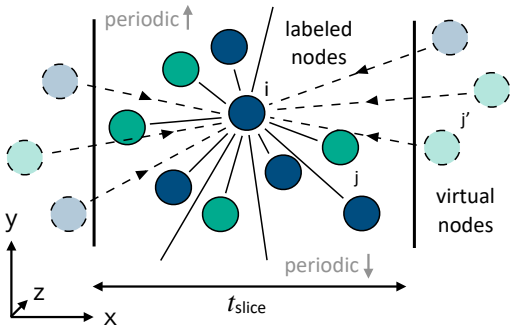

Figure 4: Illustration of how connectivity beyond the partition boundaries is incorporated, using one-way masked virtual edges ($e_{j'\to i}$) from masked virtual nodes (j') to the labeled nodes. Edges between nodes within the partition are two-way ($e_{j\leftrightarrow i}$). A set of edges from labeled and virtual nodes is shown for a single node (i) within the partition. The solid vertical lines are the partition boundaries. Different colors represent different atomic species.

Neighborhood sampling techniques such as ClusterGCN (Chiang et al. (2019)) represent an alternative, but they sacrifice the exact connectivity of the graph to enable computational efficiency and scalability. As $\boldsymbol{H}$ is a function of the relative positions and species of all constituent atoms, directly changing the representation of local atomic neighborhoods compromises the achievable accuracy. Omitting any connections leads to misinformation and poor generalization, as the network tries to fit to the target data while aggregating information through an incorrect/incomplete graph structure.

Training of large GNNs for electronic property prediction thus necessitates new strategies to become computationally feasible.

To enable efficient training of the graph while maintaining correct atomic environments and neighboring edge connections, we introduce an *augmented partitioning* approach. A visual representation of it is provided in **Fig. 4**. The graph is partitioned into slices along the x-axis (longest dimension), and maintains periodic edges across the y- and z-boundaries. Each slice contains atoms and edges within a fixed interval between x_0 and $x_0 + t_{slice}$, where x_0 and t_{slice} are the starting x-coordinate and length of the slice, respectively. Atoms outside of a given slice but present in the connectivity lists of those within are represented by virtual nodes (**Fig. 4** - dashed circles). They are connected to the slice using one-way virtual edges (**Fig. 4** - dashed lines). Details about the construction of partitions are given in **Appendix C**.

These virtual nodes/edges are initialized similarly to their labeled counterparts with input atomic numbers and distances. However, their outputs are masked and omitted from the loss computation during training, validation, and inference. Our masking approach differs from the one used in transductive learning schemes, where the objective is to learn the outputs of masked nodes/edges (Kipf & Welling (2016)). Here, we do not attempt to learn or predict their outputs. The purpose of masked nodes and edges here is to inform each partition of its full connectivity and thus provide a much closer representation of the graph topology. As the set of virtual connections used to augment each graph corresponds only to the 1-hop neighborhood, we include only 1 MP layer in the network. During message passing, the network can then learn an accurate and generalizable aggregation function when fitting to the output values of the labeled nodes and edges. Hence, the network trained on a batch of such slices can predict the full graph of an unseen test structure.

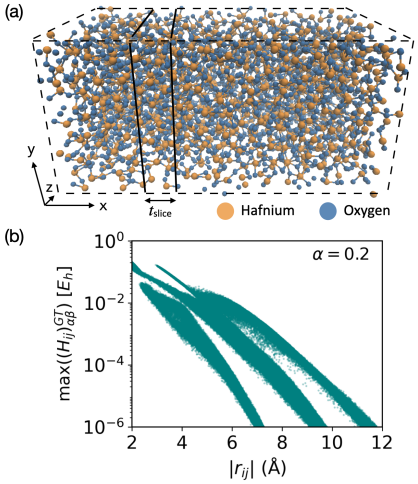

Figure 5: (a) Example atomic structure of a-HfO_2, showing oxygen atoms in blue and hafnium atoms in orange. The unit cell, which is illustrated by the black dashed box, has x-, y-, and z-dimensions of 53.876 Å $\times$ 26.308 Å $\times$ 26.242 Å, respectively. A slice (partition), characterized by a length t_{slice}, is also illustrated. (b) Distribution of the maximum element of each block of $\boldsymbol{H}$ as a function of interatomic distance, demonstrating the near-sighted nature of orbital interactions.

3.3 A-HfO_2 STRUCTURE CREATION

To generate sufficiently rich training data, existing datasets typically sample molecules at various time steps of molecular dynamics (MD) trajectories (Yu et al. (2023a); Schütt et al. (2019); Christensen & lilienfeld (2020)) or generate multiple small perturbations of the atoms in a crystalline lattice (Li et al. (2022)). In the case of amorphous crystals, we take advantage of the fact that (1) almost each node has a different local atomic environment, and (2) the structure contains a large sampling of different motifs. A wide range of training data can thus be captured within a single sample. We, therefore, generated a dataset of only three unique amorphous HfO_2 (a-HfO_2) structures for training, validation, and testing, respectively. The DFT-based Hamiltonian of each of these systems ($\boldsymbol{H}^{GT}$) was computed with a single-ζ valence (SZV) basis with 10 (4) Gaussian orbitals per Hf (O) atom. Details of the structure generation can be found in **Appendix F.1**. A structure example is shown in **Fig. 5**.

Structure	# atoms	# orbitals	# edges	x [Å]	y [Å]	z [Å]	nnz_H
1-validation	3,000	18,000	527,348	52.876	26.308	26.242	28,625,310
2-training	3,000	18,000	533,364	52.346	26.237	26.293	28,943,862
3-testing	3,000	18,000	530,920	52.722	26.267	26.191	28,805,422

Table 1: Attributes of the three generated a-HfO_2 structures: The $[x, y, z]$ triplet defines the periodic unit cell size. nnz_H is the number of non-zero elements in the Hamiltonian, encompassing all orbital interactions. Edges were defined according to an interaction distance of r_{cut} = 8 Å.

4 RESULTS

For fair comparisons in experiments where the quantity of training data varies, we used a ReduceLRonPlateau scheduler that tracks the validation loss per epoch and reduces the learning rate by a fixed decay factor when no further decrease is detected. Training is stopped once a minimum learning rate is reached. Details on the values of the hyperparameters and the scheduler settings for different experiments can be found in **Appendix E**.

When trained on the $(H_{i,j})_{\alpha,\beta}$ elements of H_2O molecules from the MD17 dataset (Schütt et al. (2019)), our network as detailed in **Appendix A** can achieve prediction accuracy within an order of magnitude (100 $\times 10^{-6} E_h$ (E_h = Hartree) vs. $\sim$10 $\times 10^{-6} E_h$) of state-of-the-start equivariant GNN approaches, while using fewer layers (2 vs. 4-5) (**Appendix B**).

The treatment of the a-HfO_2 structures is, however, more challenging. We test the model's ability to generalize to different configurations of this system by predicting $\boldsymbol{H}$ of the third structure in **Table 1**, which remains unseen during the training process. The *augmented partitioning* scheme is only applied during training (on structure 2), while the $\boldsymbol{H}$ of the unseen structure as a single graph, including all nodes and edges, is predicted during inference (structure 3). Errors are reported separately for nodes (ϵ_n) and edges (ϵ_e) for a more complete analysis that distinguishes intra- and inter-atomic orbital interactions, which have very different magnitudes. Considering the large number of different motifs in the disordered structure, we also report the standard deviation of the node and edge errors (σ_n and σ_e) to provide information on the consistency of the predictions.

4.1 CUTOFF RADIUS AND CONNECTIVITY

We first explore the minimal graph connectivity that can be used by the network to accurately learn relevant features. To do this we use the slice partition approach introduced in **Section 3.2**, using a single slice of length t_{slice} = 3 Å to train the network. Reducing the value of r_{cut} below 8 Å noticeably increases the error ($\epsilon_{\mathbf{n/e}}$), thus demonstrating the sensitivity of $\boldsymbol{H}$ to the exact connectivity of the graph. Going from r_{cut} = 8 Å to 10 Å , the prediction error begins to plateau, but the node degree (which is proportional to the memory consumption of the network) grows by 1.7$\times$. An r_{cut} of 8 Å also results in negligible changes to the eigenvalue spectra (**Fig. 10** in **Appendix F.1**). We thus set r_{cut}=8 Å when defining graph edges for subsequent experiments. Note that $\epsilon_{node} >> \epsilon_{edge}$ as the magnitude of the node labels is $\sim$100$\times$ larger than that of the edge labels.

r_{cut} [Å]	$deg(n)$	$deg(n)'$	Epochs	$\epsilon_{\mathbf{n}}$	$\sigma_{\mathbf{n}}$	$\epsilon_{\mathbf{e}}$	$\sigma_{\mathbf{e}}$
4	20.99	10.81	13,816	4.14	0.00960	9.60	0.00105
6	74.23	27.78	14,071	3.79	0.00925	0.40	0.00074
8	177.09	51.17	18,245	3.76	0.00903	0.22	0.00050
10	346.03	81.25	22,463	3.76	0.00886	0.15	0.00040

Table 2: Prediction accuracy of the network with different r_{cut}. Training was done with a single slice of length t_{slice} = 3 Å taken from structure 2 at x_0 = 25 Å. The edge connectivity of the matrix is set by r_{cut}. $deg(n)$ is the average node degree, and $deg(n)'$ the reduced node degree omitting virtual node neighbors. Note that for this value of t_{slice}, the majority of neighbors for the average node are virtual. ϵ_n and ϵ_e are the Mean Average Error (MAE) for nodes/edges, respectively, and σ_n and σ_e are the corresponding standard deviations. All units are in [$\times 10^{-3} E_h$]. In all cases, one MP layer is used. The validation loss of the model is computed from a slice of similar length, interaction distance, and starting location extracted from structure 1. The networks are tested on an unseen full graph (structure 3) constructed with the same r_{cut}.

4.2 ABLATION STUDIES OF THE TRAINING APPROACH

Next, we perform a study on the design features of the *augmented partitioning* approach introduced in **Section 3.2**. In particular, we examine the influence of virtual nodes, one-way/two-way, and one/two MP layers on the prediction accuracy. **Table 3** compiles ablation studies of the three aforementioned parameters, using 18 slices of length t_{slice} = $\sim$3 Å that cover the full training structure (structure 2).

Compared to training with raw partitions, the addition of virtual nodes and edges reduces both ϵ_{node} and ϵ_{edge} by over $\sim$50% when evaluated on the full test structure. Such an improvement is

Edges	# MP	$\epsilon_\mathbf{n}$	$\sigma_\mathbf{n}$	$\epsilon_\mathbf{e}$	$\sigma_\mathbf{e}$
$n' \quad n$	1	5.18	7.93	1.66	0.0026
$n' \rightarrow n$	1	2.29	5.09	0.20	0.0038
$n' \leftrightarrow n$	1	2.38	5.26	0.23	0.0042
$n' \rightarrow n$	2	8.60	21.01	0.24	0.0043
$n' \leftrightarrow n$	2	8.44	20.65	0.24	0.0041

Table 3: Ablation studies exploring the impact of virtual nodes, one-way edges, and # of MP layers on the prediction accuracy when tested on structure 3, using slices of length t_{slice} = 3 Å from structure 2 for training and of length t_{slice} = 4 Å (taken at $x_0 = 25$ Å) from structure 1 for validation. The first column indicates the edge direction between virtual (n') and labeled (n) nodes. $n' \rightarrow n$ are one-way (incoming) edges, while $n' \leftrightarrow n$ are two-way edges. Values are reported in $\epsilon_n[mE_h]$ and $\sigma_n[\mu E_h]$.

t_{slice} [Å]	N_t	N_e	Epochs	$\epsilon_\mathbf{n}$	$\sigma_\mathbf{n}$	$\epsilon_\mathbf{e}$	$\sigma_\mathbf{e}$
$\sim$1	54	47,958	15,744	2.30	5.37	0.20	0.37
$\sim$2	27	95,398	15,628	2.32	5.19	0.20	0.36
$\sim$3	18	141,512	15,675	2.29	5.09	0.20	0.38
$\sim$4	14	184,730	14,833	2.45	5.47	0.21	0.38
$\sim$8	7	320,324	20,599	2.45	5.41	0.17	0.34
$\sim$12	5	381,504	19,351	2.59	5.86	0.18	0.36
$\sim$52	1	533,364	23,396	2.46	5.39	0.16	0.33

Table 4: Prediction accuracy when the network is trained on differently-sized partitions of the same graph (structure 2), using 1 MP layer. N_e = # of slices, N_e = total # of labeled edges. The total number of labeled nodes remains constant. The number of slices is equal to $\sim L/t$, where L = 52.346 Å is the full length of structure 2 used for training. The validation set is a slice of length t_{slice} = 4 Å starting at x_0 = 25 Å from structure 1. The models are tested on the full unseen structure (structure 3) and values are reported in $\epsilon_n[mE_h]$ and $\sigma_n[\mu E_h]$.

expected, as raw partitions are characterized by a large proportion of missing edges. We note that the best performing case achieves an ϵ_n and ϵ_e of 2.29 $\times 10^{-3} E_h$ and 0.20 $\times 10^{-3} E_h$, respectively, using a single MP layer and one-way edges from virtual to labeled nodes ($n' \rightarrow n$). As $t_{slice} < r_{cut}$, a one-hop neighborhood is sufficient to cover all nodes across a partition. This property renders a single MP layer sufficient, considering the near-sightedness of the Hamiltonian. The single MP-network's performance is trivially unaffected by the use of one-way virtual edges rather than two ($n' \leftrightarrow n$); virtual nodes do not need to aggregate information as they are omitted from the loss. The edges connecting the labeled to virtual nodes ($n \rightarrow n'$) can thus be omitted to reduce memory consumption. Using 2 MP layers with one layer of virtual nodes, however, degrades the performance as the 2-hop neighborhood is not correctly represented. It should be emphasized that the full graph with 2 MP layers does not fit into the memory of a single NVIDIA A100 GPU (requiring $>$ 80 GiB). Results with 2 MP layers are in **Appendix D** (under **Table 9**).

4.2.1 Effect of augmented partitioning on prediction accuracy

The *augmented partitioning* approach introduced in **Section 3.2** allows for the subdivision of the large graphs associated with the training of disordered materials by defining small slices (i.e., small t_{slice}) that can be treated sequentially on a single GPU or distributed across multiple GPUs and processed independently in parallel. Intermediate quantities do not need to be communicated during the forward/backward passes.

To establish that the network trained on augmented partitions does not suffer from loss of accuracy, we partition the same full graph into different numbers of slices with different thicknesses for training. In each case, the total number of labeled atoms summed up across all the slices remains the same (3,000), while the total number of labeled edges reduces with increasing partitions. From **Table 4** it can be seen that the prediction error is insensitive to partition size. Despite the different divisions ranging from 5 (t_{slice} = $\sim$12 Å) to 54 (t_{slice} = $\sim$1 Å) slices, $\epsilon_\mathbf{n}$ and $\epsilon_\mathbf{e}$ remain very close to the values obtained by training with the full graph (t_{slice} = 52.346 Å). For small slices, the reduced fraction of labeled connections along the x direction does not affect the accuracy as the remaining data along the y and z directions is sufficient to train the network. The combined MAE loss from all 3,000 atoms and 530,920 edges for the best performing case (t_{slice} = $\sim$3 Å) is 0.2159 mE_h, or 5.87 meV. This value is comparable to what a previous study obtained (2.2 meV) using equivariant GNNs for much smaller structures with $\leq$150 atoms per unit cell (Wang et al. (2024b)).

4.3 Performance on a-HfO_2

To assess whether the prediction accuracy of the trained network is sufficient for practical application, we assemble the full Hamiltonian of the a-HfO_2 test structure using the network outputs ($\boldsymbol{H}^{pred}$), extract key quantities, and compare them with results obtained from the ground-truth

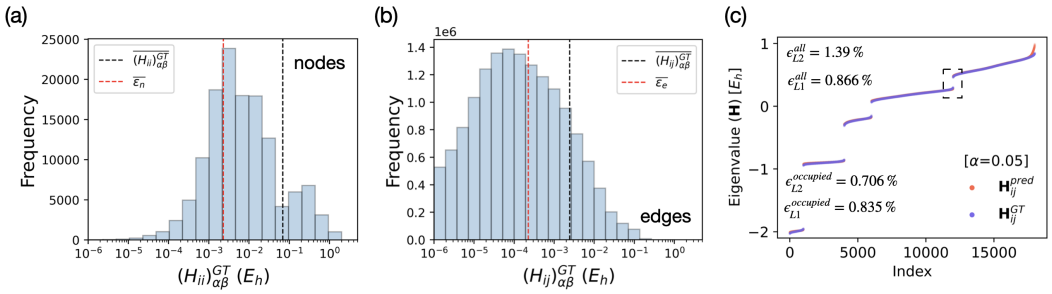

Figure 6: (a) ϵ_n of the predicted node blocks (red dashed lines) plotted against the full distribution of entries in the ground-truth Hamiltonian matrix $(H_{i,j})^{GT}_{\alpha,\beta}$. (b) Same as (a), but for ϵ_e of the predicted edge blocks. (c) Eigenvalue spectra of the predicted ($\boldsymbol{H}^{pred}$) and reference ($\boldsymbol{H}^{GT}$) Hamiltonian matrices. The alpha value indicates the scatter point transparency, such that the differences between the two scatter point sets can be more clearly seen. $(\boldsymbol{H}_{i,j})^{pred}$ is symmetrized before diagonalization with $\boldsymbol{H} = \frac{1}{2}(\boldsymbol{H} + \boldsymbol{H}^{\dagger})$. The relative L1/L2 errors in the eigenvalue spectra, computed as $(\|(\vec{E})^{pred} - (\vec{E})^{GT}\|^2_{norm})/(\|(\vec{E})^{GT}\|^2_{norm})$ (norm = 1, 2) where $\vec{E}$ is the vector of eigenvalues, are also shown for all eigenvalues and the ones corresponding to occupied states (below 0.305 E_h). The black dashed box indicates the bandgap, which is defined as the difference between the first energy above and below the Fermi level.

Hamiltonian ($\boldsymbol{H}^{GT}$) computed with DFT. In **Fig. 6** we show the achieved ϵ_n and ϵ_e relative to the magnitude of the $\boldsymbol{H}^{GT}$ entries. We then compute the eigenvalue spectrum of $\boldsymbol{H}^{pred}$ and $\boldsymbol{H}^{GT}$ as well as the error distribution between them. The network used to create $\boldsymbol{H}^{pred}$ was trained with 18 partitions of length t_{slice} = ∼3 Å. We observe that both ϵ_n and ϵ_e are at least one order of magnitude lower than the average matrix element corresponding to the diagonal/off-diagonal blocks of the Hamiltonian (black dashed line). This allows for the reconstructed $\boldsymbol{H}^{pred}$ to reproduce all eigenvalues of $\boldsymbol{H}^{GT}$ within 0.87% relative L1 error. The error is 0.84% when eigenvalues of unoccupied states above the cutoff 0.306 E_h are excluded. The remaining error is carried mostly by the largest eigenvalues, and distributed around the edges of energy gaps (see **Fig. 13** in **Appendix H**), which correspond to regimes of stronger inter-atomic orbital coupling (Atkins & De Paula (2009)).

4.4 Computational cost

Compared to a naive full-batch training of the graph, our method using just 8 augmented slices results in a 6.5× speedup per epoch (0.38 vs. 2.5 s), and a 7.2× decrease in memory consumption per rank (8.59 vs. 61.68 GiB). A more complete analysis is provided in **Appendix G.2**. This scaling behavior is limited only by the overhead introduced by the virtual nodes/edges, and the small computational load imbalance from partitioning. Further computational improvements could be achieved by combining the augmentation approach with optimized graph partitioning algorithms (Karypis & Kumar (1998)) while leveraging periodicity.

The extension of GNN-based predictions to large material systems could potentially save tremendous amounts of computational time. While DFT calculations to obtain the $\boldsymbol{H}^{GT}$ of small molecules (e.g., H_2O) take only a few seconds, the same operation for a-HfO_2 structures made of 3,000 atoms is computationally ∼100× heavier (∼0.04 vs. ∼3.65 node hours, see **Appendix G**). More importantly, the GNN prediction unlocks the ability to consider much larger structures than the ones considered here, the inference phase scaling with $\mathcal{O}(N_{atoms})$ while DFT calculations are limited to $\mathcal{O}(N^3_{atoms})$. The model could also serve as an initial guess to DFT packages to reduce the number of self-consistent field iterations that are required to obtain converged electron densities (Unke et al. (2021)).

5 Conclusion

We adapted equivariant GNNs to learn the electronic properties of amorphous materials, and introduced an *augmented partitioning* approach to break down and train the large graphs encountered when dealing with realistic structural disorder, without sacrificing accuracy. More generally, we proposed a method to tackle the training of atomic systems that require large, highly connected, and

near-sighted graphs, and for which a single MP layer can be sufficient. The key is the addition of virtual nodes and edges connected to relatively small partitions that mimic their neighborhood. The method, demonstrated here on a-HfO_2, can be straightforwardly applied to other disordered materials, or adapted to learn their other rotationally-equivariant attributes such as vibrational properties, e.g., phonon dispersions (Fang et al. (2024)).

The resulting networks capture relevant properties of a-HfO_2 in sufficient detail to achieve few-meV accuracy and reproduce features of practical relevance, such as the energy eigenvalues. However, the sub-millielectronvolt range is not currently reached, contrary to what has been demonstrated with small-molecule datasets (Yu et al. (2023b); Unke et al. (2021)). This shortcoming can most likely be attributed to a combination of greater dataset complexity in amorphous compounds, coarser resolution of the training data ($\epsilon_{SCF} = 1 \times 10^{-6} E_h$), and limited network size. Further data generation, parameter optimization, and enabling of networks with increased expressiveness will be the next steps.

5.1 Outlook & Applications

The ability to learn the electronic properties of complex disordered materials unlocks notable applications in computational physics, chemistry, and materials science. Several compounds are used in their amorphous phase, as they often exhibit different properties from their crystalline equivalents. For example, a-SiO_2 as dielectric layer has been a key enabler of the metal-oxide-semiconductor technology (Nekrashevich & Gritsenko (2014)), IGZO, thanks to its large electron mobility, serves as channel of flexible transistors (Kamiya et al. (2010)), a-HfO_2 allows for the (non-)volatile storage of information, when placed between two metallic electrodes (Chan et al. (2008)), and GST can be used to write/store data optically (Pirovano et al. (2004); Kolobov et al. (2004)). Downscaling of materials also reveals structural effects similar to disorder, e.g., defects (Wilhelmer et al. (2022)), strain Parton & Verheyen (2006), or grain boundaries (Weitz et al. (2009)). All of them require large unit cells to be accurately described (Lany & Zunger (2008); Zhao et al. (2020)). Computationally expensive DFT calculations represent a bottleneck towards investigating the electronic properties of such systems in simulations. Recent advances in graph neural networks, combined with domain-specific innovations to train them, will enable such explorations.

Author Contributions

[anonymized]

Acknowledgments

[anonimized]

Reproducibility

The code used to set up and train the network is available at the following repository: [anonymized code temporarily provided as supplementary material]. CP2K was used to generate the custom HfO_2 dataset. Input files are provided in the same repository.

References

Vladimir I. Anisimov, Jan Zaanen, and Ole K. Andersen. Band theory and mott insulators: Hubbard u instead of stoner i. *Physical Review B*, 44:943–954, Jul 1991.

Peter Atkins and Julio De Paula. *Atkins' physical chemistry*. Oxford University Press, London, England, 9 edition, November 2009.

Hexin Bai, Peng Chu, Jeng-Yuan Tsai, Nathan Wilson, Xiaofeng Qian, Qimin Yan, and Haibin Ling. Graph neural network for hamiltonian-based material property prediction. *Neural Computing and Applications*, 34(6):4625–4632, November 2021. ISSN 1433-3058. doi: 10.1007/s00521-021-06616-0. URL http://dx.doi.org/10.1007/s00521-021-06616-0.

Ilyes Batatia, Lars L. Schaaf, Huajie Chen, Gábor Csányi, Christoph Ortner, and Felix A. Faber. Equivariant matrix function neural networks, 2023. URL https://arxiv.org/abs/2310.10434.

Maciej Besta and Torsten Hoefler. Parallel and distributed graph neural networks: An in-depth concurrency analysis. *IEEE Transactions on Pattern Analysis and Machine Intelligence*, 46(5): 2584–2606, May 2024. ISSN 1939-3539. doi: 10.1109/tpami.2023.3303431. URL http://dx.doi.org/10.1109/TPAMI.2023.3303431.

M.Y. Chan, T. Zhang, V. Ho, and P.S. Lee. Resistive switching effects of hfo2 high-k dielectric. *Microelectronic Engineering*, 85(12):2420–2424, December 2008. ISSN 0167-9317. doi: 10.1016/j.mee.2008.09.021. URL http://dx.doi.org/10.1016/j.mee.2008.09.021.

Wei-Lin Chiang, Xuanqing Liu, Si Si, Yang Li, Samy Bengio, and Cho-Jui Hsieh. Cluster-gcn: An efficient algorithm for training deep and large graph convolutional networks. In *Proceedings of the 25th ACM SIGKDD International Conference on Knowledge Discovery amp; Data Mining*, KDD '19. ACM, July 2019. doi: 10.1145/3292500.3330925. URL http://dx.doi.org/10.1145/3292500.3330925.

J.H. Choi, Y. Mao, and J.P. Chang. Development of hafnium based high-k materials—a review. *Materials Science and Engineering: R: Reports*, 72(6):97–136, July 2011. ISSN 0927-796X. doi: 10.1016/j.mser.2010.12.001. URL http://dx.doi.org/10.1016/j.mser.2010.12.001.

Anders S. Christensen and Anatole Von lilienfeld. Revised MD17 dataset (rMD17). 7 2020. doi: 10.6084/m9.figshare.12672038.v3. URL https://figshare.com/articles/dataset/Revised_MD17_dataset_rMD17_/12672038.

Ralf Drautz. Atomic cluster expansion of scalar, vectorial, and tensorial properties including magnetism and charge transfer. *Physical Review B*, 102(2), July 2020. ISSN 2469-9969. doi: 10.1103/physrevb.102.024104. URL http://dx.doi.org/10.1103/PhysRevB.102.024104.

Fabian Ducry, Jan Aeschlimann, and Mathieu Luisier. Electro-thermal transport in disordered nanostructures: a modeling perspective. *Nanoscale Advances*, 2(7):2648–2667, 2020. ISSN 2516-0230. doi: 10.1039/d0na00168f. URL http://dx.doi.org/10.1039/d0na00168f.

Shiang Fang, Mario Geiger, Joseph G. Checkelsky, and Tess Smidt. Phonon predictions with e(3)-equivariant graph neural networks, 2024. URL https://arxiv.org/abs/2403.11347.

Xiaoxun Gong, He Li, Nianlong Zou, Runzhang Xu, Wenhui Duan, and Yong Xu. General framework for e(3)-equivariant neural network representation of density functional theory hamiltonian. *Nature Communications*, 14(1), May 2023. ISSN 2041-1723. doi: 10.1038/s41467-023-38468-8. URL http://dx.doi.org/10.1038/s41467-023-38468-8.

Qiangqiang Gu, Zhanghao Zhouyin, Shishir Kumar Pandey, Peng Zhang, Linfeng Zhang, and Weinan E. Deep learning tight-binding approach for large-scale electronic simulations at finite temperatures with ab initio accuracy. *Nature Communications*, 15(1), August 2024. ISSN 2041-1723. doi: 10.1038/s41467-024-51006-4. URL http://dx.doi.org/10.1038/s41467-024-51006-4.

Ganesh Hegde and R. Chris Bowen. Machine-learned approximations to density functional theory hamiltonians. *Scientific Reports*, 7(1), February 2017. ISSN 2045-2322. doi: 10.1038/srep42669. URL http://dx.doi.org/10.1038/srep42669.

P. Hohenberg and W. Kohn. Inhomogeneous electron gas. *Physical Review*, 136(3B):B864–B871, November 1964. ISSN 0031-899X. doi: 10.1103/physrev.136.b864. URL http://dx.doi.org/10.1103/PhysRev.136.B864.

Toshio Kamiya, Kenji Nomura, and Hideo Hosono. Present status of amorphous in–ga–zn–o thin-film transistors. *Science and Technology of Advanced Materials*, 11(4):044305, February 2010. ISSN 1878-5514. doi: 10.1088/1468-6996/11/4/044305. URL http://dx.doi.org/10.1088/1468-6996/11/4/044305.

Manasa Kaniselvan, Mathieu Luisier, and Marko Mladenović. An atomistic model of field-induced resistive switching in valence change memory. *ACS Nano*, 17(9):8281–8292, March 2023. ISSN 1936-086X. doi: 10.1021/acsnano.2c12575. URL http://dx.doi.org/10.1021/acsnano.2c12575.

George Karypis and Vipin Kumar. A parallel algorithm for multilevel graph partitioning and sparse matrix ordering. *Journal of Parallel and Distributed Computing*, 48(1):71–95, January 1998. ISSN 0743-7315. doi: 10.1006/jpdc.1997.1403. URL http://dx.doi.org/10.1006/jpdc.1997.1403.

Thomas N. Kipf and Max Welling. Semi-supervised classification with graph convolutional networks. *CoRR*, abs/1609.02907, 2016. URL http://arxiv.org/abs/1609.02907.

Cedric Klinkert, Áron Szabó, Christian Stieger, Davide Campi, Nicola Marzari, and Mathieu Luisier. 2-d materials for ultrascaled field-effect transistors: One hundred candidates under the ab initio microscope. *ACS Nano*, 14(7):8605–8615, June 2020. ISSN 1936-086X. doi: 10.1021/acsnano.0c02983. URL http://dx.doi.org/10.1021/acsnano.0c02983.

W. Kohn and L. J. Sham. Self-consistent equations including exchange and correlation effects. *Physical Review*, 140(4A):A1133–A1138, November 1965. ISSN 0031-899X. doi: 10.1103/physrev.140.a1133. URL http://dx.doi.org/10.1103/PhysRev.140.A1133.

Alexander V. Kolobov, Paul Fons, Anatoly I. Frenkel, Alexei L. Ankudinov, Junji Tominaga, and Tomoya Uruga. Understanding the phase-change mechanism of rewritable optical media. *Nature Materials*, 3(10):703–708, September 2004. ISSN 1476-4660. doi: 10.1038/nmat1215. URL http://dx.doi.org/10.1038/nmat1215.

Thomas D. Kühne, Marcella Iannuzzi, Mauro Del Ben, Vladimir V. Rybkin, Patrick Seewald, Frederick Stein, Teodoro Laino, Rustam Z. Khaliullin, Ole Schütt, Florian Schiffmann, Dorothea Golze, Jan Wilhelm, Sergey Chulkov, Mohammad Hossein Bani-Hashemian, Valéry Weber, Urban Borštnik, Mathieu Taillefumier, Alice Shoshana Jakobovits, Alfio Lazzaro, Hans Pabst, and *et al.* CP2k: An electronic structure and molecular dynamics software package - quickstep: Efficient and accurate electronic structure calculations. *J. Chem. Phys.*, 152(19):194103, May 2020.

Stephan Lany and Alex Zunger. Assessment of correction methods for the band-gap problem and for finite-size effects in supercell defect calculations: Case studies for zno and gaas. *Physical Review B*, 78(23), December 2008. ISSN 1550-235X. doi: 10.1103/physrevb.78.235104. URL http://dx.doi.org/10.1103/PhysRevB.78.235104.

He Li, Zun Wang, Nianlong Zou, Meng Ye, Runzhang Xu, Xiaoxun Gong, Wenhui Duan, and Yong Xu. Deep-learning density functional theory hamiltonian for efficient ab initio electronic-structure calculation. *Nature Computational Science*, 2(6):367–377, June 2022. ISSN 2662-8457. doi: 10.1038/s43588-022-00265-6. URL http://dx.doi.org/10.1038/s43588-022-00265-6.

Shen Li, Yanli Zhao, Rohan Varma, Omkar Salpekar, Pieter Noordhuis, Teng Li, Adam Paszke, Jeff Smith, Brian Vaughan, Pritam Damania, and Soumith Chintala. Pytorch distributed: Experiences on accelerating data parallel training, 2020. URL https://arxiv.org/abs/2006.15704.

Renjie Liao, Marc Brockschmidt, Daniel Tarlow, Alexander L. Gaunt, Raquel Urtasun, and Richard Zemel. Graph partition neural networks for semi-supervised classification, 2018. URL https://arxiv.org/abs/1803.06272.

Yi-Lun Liao, Brandon Wood, Abhishek Das, and Tess Smidt. Equiformerv2: Improved equivariant transformer for scaling to higher-degree representations, 2023. URL https://arxiv.org/abs/2306.12059.

Frank Neese. The orca program system. *WIREs Computational Molecular Science*, 2(1):73–78, June 2011. ISSN 1759-0884. doi: 10.1002/wcms.81. URL http://dx.doi.org/10.1002/wcms.81.

S. S. Nekrashevich and V. A. Gritsenko. Electronic structure of silicon dioxide (a review). *Physics of the Solid State*, 56(2):207–222, February 2014. ISSN 1090-6460. doi: 10.1134/s106378341402022x. URL http://dx.doi.org/10.1134/S106378341402022X.

Jigyasa Nigam, Michael J. Willatt, and Michele Ceriotti. Equivariant representations for molecular hamiltonians and n-center atomic-scale properties. *The Journal of Chemical Physics*, 156(1), January 2022. ISSN 1089-7690. doi: 10.1063/5.0072784. URL http://dx.doi.org/10.1063/5.0072784.

Els Parton and Peter Verheyen. Strained silicon — the key to sub-45 nm cmos. *III-Vs Review*, 19 (3):28–31, April 2006. ISSN 0961-1290. doi: 10.1016/s0961-1290(06)71590-3. URL http://dx.doi.org/10.1016/S0961-1290(06)71590-3.

Saro Passaro and C. Lawrence Zitnick. Reducing so(3) convolutions to so(2) for efficient equivariant gnns, 2023. URL https://arxiv.org/abs/2302.03655.

John P. Perdew, Kieron Burke, and Matthias Ernzerhof. Generalized gradient approximation made simple [phys. rev. lett. 77, 3865 (1996)]. *Phys. Rev. Lett.*, 78:1396–1396, Feb 1997.

A. Pirovano, A.L. Lacaita, A. Benvenuti, F. Pellizzer, and R. Bez. Electronic switching in phase-change memories. *IEEE Transactions on Electron Devices*, 51(3):452–459, March 2004. ISSN 0018-9383. doi: 10.1109/ted.2003.823243. URL http://dx.doi.org/10.1109/TED.2003.823243.

Chendi Qian, Andrei Manolache, Christopher Morris, and Mathias Niepert. Probabilistic graph rewiring via virtual nodes, 2024. URL https://arxiv.org/abs/2405.17311.

Gil M. Repa and Lisa A. Fredin. Predicting electronic structure of realistic amorphous surfaces. *Advanced Theory and Simulations*, 6(11), June 2023. ISSN 2513-0390. doi: 10.1002/adts.202300292. URL http://dx.doi.org/10.1002/adts.202300292.

K. T. Schütt, M. Gastegger, A. Tkatchenko, K.-R. Müller, and R. J. Maurer. Unifying machine learning and quantum chemistry with a deep neural network for molecular wavefunctions. *Nature Communications*, 10(1), November 2019. ISSN 2041-1723. doi: 10.1038/s41467-019-12875-2. URL http://dx.doi.org/10.1038/s41467-019-12875-2.

M. L. Senent and S. Wilson. Intramolecular basis set superposition errors. *International Journal of Quantum Chemistry*, 82(6):282–292, 2001. doi: https://doi.org/10.1002/qua.1030. URL https://onlinelibrary.wiley.com/doi/abs/10.1002/qua.1030.

Jack Strand, Moloud Kaviani, David Gao, Al-Moatasem El-Sayed, Valeri V Afanas'ev, and Alexander L Shluger. Intrinsic charge trapping in amorphous oxide films: status and challenges. *Journal of Physics: Condensed Matter*, 30(23):233001, May 2018. ISSN 1361-648X. doi: 10.1088/1361-648x/aac005. URL http://dx.doi.org/10.1088/1361-648X/aac005.

Anders Blom Troels Markussen Jess Wellendorff Julian Schneider Tue Gunst Brecht Verstichel Petr A Khomyakov Ulrik G Vej-Hansen Mads Brandbyge Søren Smidstrup, Kurt Stokbro et al. Quantumatk: An integrated platform of electronic and atomic-scale modelling tools. *J. Phys: Condens. Matter (APS)*, 32:015901, 2020. doi: 10.1088/1361-648X/ab4007. URL https://iopscience.iop.org/article/10.1088/1361-648X/ab4007.

De Nyago Tafen and D. A. Drabold. Realistic models of binary glasses from models of tetrahedral amorphous semiconductors. *Physical Review B*, 68(16), October 2003. ISSN 1095-3795. doi: 10.1103/physrevb.68.165208. URL http://dx.doi.org/10.1103/PhysRevB.68.165208.

Nathaniel Thomas, Tess Smidt, Steven Kearnes, Lusann Yang, Li Li, Kai Kohlhoff, and Patrick Riley. Tensor field networks: Rotation- and translation-equivariant neural networks for 3d point clouds, 2018. URL https://arxiv.org/abs/1802.08219.

Oliver T. Unke, Mihail Bogojeski, Michael Gastegger, Mario Geiger, Tess Smidt, and Klaus-Robert Müller. Se(3)-equivariant prediction of molecular wavefunctions and electronic densities, 2021. URL https://arxiv.org/abs/2106.02347.

M. Laura Urquiza, Md Mahbubul Islam, Adri C. T. van Duin, Xavier Cartoixà, and Alejandro Strachan. Atomistic insights on the full operation cycle of a hfo2-based resistive random access memory cell from molecular dynamics. *ACS Nano*, 15(8):12945–12954, July 2021. ISSN 1936-086X. doi: 10.1021/acsnano.1c01466. URL http://dx.doi.org/10.1021/acsnano.1c01466.

Joost VandeVondele and Jürg Hutter. Gaussian basis sets for accurate calculations on molecular systems in gas and condensed phases. *J. Chem. Phys.*, 127(11):114105, 09 2007. ISSN 0021-9606.

Petar Veličković, Guillem Cucurull, Arantxa Casanova, Adriana Romero, Pietro Liò, and Yoshua Bengio. Graph Attention Networks. In *ICLR*, 2018.

Cheng Wan, Youjie Li, Cameron R Wolfe, Anastasios Kyrillidis, Nam Sung Kim, and Yingyan Lin. PipeGCN: Efficient full-graph training of graph convolutional networks with pipelined feature communication. March 2022.

Yuxiang Wang, He Li, Zechen Tang, Honggeng Tao, Yanzhen Wang, Zilong Yuan, Zezhou Chen, Wenhui Duan, and Yong Xu. Deeph-2: Enhancing deep-learning electronic structure via an equivariant local-coordinate transformer, 2024a. URL https://arxiv.org/abs/2401.17015.

Yuxiang Wang, Yang Li, Zechen Tang, He Li, Zilong Yuan, Honggeng Tao, Nianlong Zou, Ting Bao, Xinghao Liang, Zezhou Chen, Shanghua Xu, Ce Bian, Zhiming Xu, Chong Wang, Chen Si, Wenhui Duan, and Yong Xu. Universal materials model of deep-learning density functional theory hamiltonian. *Science Bulletin*, 69(16):2514–2521, 2024b. ISSN 2095-9273. doi: https://doi.org/10.1016/j.scib.2024.06.011. URL https://www.sciencedirect.com/science/article/pii/S2095927324004079.

Yuyang Wang, Zijie Li, and Amir Barati Farimani. *Graph Neural Networks for Molecules*, pp. 21–66. Springer International Publishing, 2023. ISBN 9783031371967. doi: 10.1007/978-3-031-37196-7_2. URL http://dx.doi.org/10.1007/978-3-031-37196-7_2.

R. T. Weitz, K. Amsharov, U. Zschieschang, M. Burghard, M. Jansen, M. Kelsch, B. Rhamati, P. A. van Aken, K. Kern, and H. Klauk. The importance of grain boundaries for the time-dependent mobility degradation in organic thin-film transistors. *Chemistry of Materials*, 21(20):4949–4954, September 2009. ISSN 1520-5002. doi: 10.1021/cm902145x. URL http://dx.doi.org/10.1021/cm902145x.

Christoph Wilhelmer, Dominic Waldhoer, Markus Jech, Al-Moatasem Bellah El-Sayed, Lukas Cvitkovich, Michael Waltl, and Tibor Grasser. Ab initio investigations in amorphous silicon dioxide: Proposing a multi-state defect model for electron and hole capture. *Microelectronics Reliability*, 139:114801, December 2022. ISSN 0026-2714. doi: 10.1016/j.microrel.2022.114801. URL http://dx.doi.org/10.1016/j.microrel.2022.114801.

Yong Youn, Youngho Kang, and Seungwu Han. An efficient method to generate amorphous structures based on local geometry. *Computational Materials Science*, 95:256–262, December 2014. ISSN 0927-0256. doi: 10.1016/j.commatsci.2014.07.053. URL http://dx.doi.org/10.1016/j.commatsci.2014.07.053.

Haiyang Yu, Meng Liu, Youzhi Luo, Alex Strasser, Xiaofeng Qian, Xiaoning Qian, and Shuiwang Ji. Qh9: A quantum hamiltonian prediction benchmark for qm9 molecules, 2023a. URL https://arxiv.org/abs/2306.09549.

Haiyang Yu, Zhao Xu, Xiaofeng Qian, Xiaoning Qian, and Shuiwang Ji. Efficient and equivariant graph networks for predicting quantum hamiltonian, 2023b. URL https://arxiv.org/abs/2306.04922.

He Zhang, Chang Liu, Zun Wang, Xinran Wei, Siyuan Liu, Nanning Zheng, Bin Shao, and Tie-Yan Liu. Self-consistency training for density-functional-theory hamiltonian prediction, 2024. URL https://arxiv.org/abs/2403.09560.

Liwei Zhang, Berk Onat, Geneviève Dusson, Adam McSloy, G. Anand, Reinhard J. Maurer, Christoph Ortner, and James R. Kermode. Equivariant analytical mapping of first principles hamiltonians to accurate and transferable materials models. *npj Computational Materials*, 8(1), July 2022. ISSN 2057-3960. doi: 10.1038/s41524-022-00843-2. URL http://dx.doi.org/10.1038/s41524-022-00843-2.

Xin-Gang Zhao, Gustavo M. Dalpian, Zhi Wang, and Alex Zunger. Polymorphous nature of cubic halide perovskites. *Physical Review B*, 101(15), April 2020. ISSN 2469-9969. doi: 10.1103/physrevb.101.155137. URL http://dx.doi.org/10.1103/PhysRevB.101.155137.

Yang Zhong, Hongyu Yu, Mao Su, Xingao Gong, and Hongjun Xiang. Transferable equivariant graph neural networks for the hamiltonians of molecules and solids. *npj Computational Materials*, 9(1), October 2023. ISSN 2057-3960. doi: 10.1038/s41524-023-01130-4. URL http://dx.doi.org/10.1038/s41524-023-01130-4.

A NETWORK ARCHITECTURE

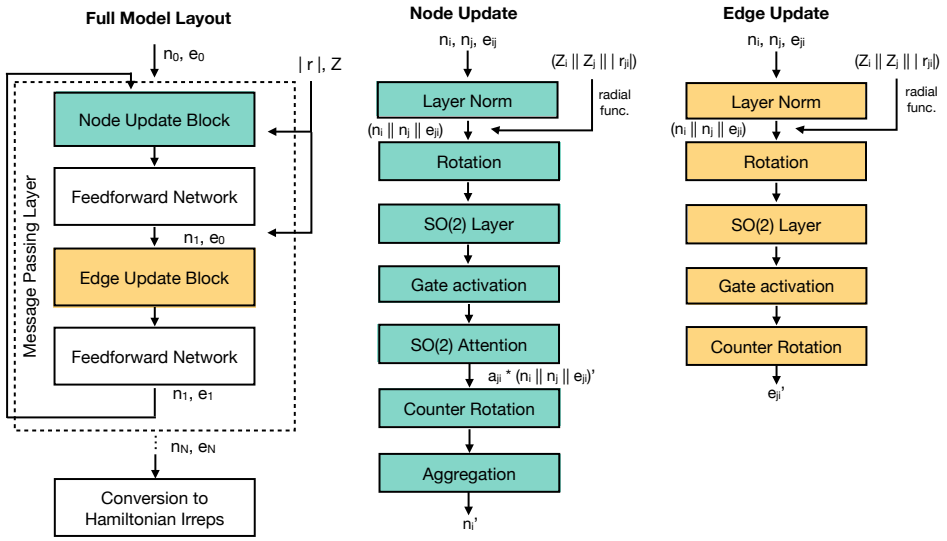

Figure 7: The node embeddings after the message passing layer labeled X are denoted as $\boldsymbol{n}_X$, and the corresponding edge features are $\boldsymbol{e}_X$. a_{ij} is the block of attention weights, Z_i is the atomic number of atom i, and r_{ij} is the scalar distance between atoms i and j. The input message to the update blocks consist of the concatenated embeddings of source and target nodes j and i, along with their connecting edge e_{ji}. They are multiplied by a set of weights generated from the radial function using a scalar embedding that consists of the atomic numbers Z_i and Z_j concatenated with the edge distance $|r_{ji}|$

In this section, we provide further details on the architecture adapted from EquiformerV2 (Liao et al. (2023)) and DeepH2 (Wang et al. (2024a)), in addition to the network initialization description in **Section 3.1**.

During message passing, input messages in the form of node embeddings of size (N_n, $(l_{max}+1)^2$, $d_{sphere,n}$) and edge embeddings of size (N_e, $(l_{max}+1)^2$, $d_{sphere,n}$) from surrounding neighboring source nodes are passed into the target node. Note that for our network, $d_{sphere,n}$ and $d_{sphere,e}$ are set to the same value d_{sphere}, known as the number of spherical channels.

Inside the node update block, the source and target atom embeddings are concatenated together with the edge embeddings of their connecting edge to form an input message of size (N_e, $(l_{max}+1)^2$, $3d_{sphere}$). The message is multiplied by weights generated by the radial functions using scalar embeddings (atomic numbers and distances), making it more receptive to small changes in environments. The dimension of these scalar embeddings are similarly set to d_{sphere}.

Afterwards, the input message is rotated to align with the z axis through the rotation block. The rotation block contains rotation matrices that were pre-computed using the normalized edge vectors of every edge in the graph. The rotated message is reshaped into m major order for linear convolutions to be performed for each $m = 0$ to $m = m_{max}$ with the number of l components for each m is given by $l_{max} - m + 1$. m_{max} and l_{max} ($m_{max} \leq l_{max}$) are other hyperparameters that can be adjusted. The convolutions produce an output embedding of size (n_e, $(l_{max}+1)^2$, d_{attn_hidden}), where attention hidden channels d_{attn_hidden} is another hyperparameter. The message is then fed through the gate activation layer, which adds non-linearity while preserving equivariance by applying separate non-linearities to the $l = 0$ and $l > 0$ components.

Next, the non-linear message is passed through a second convolution layer that produces an output embedding size of (n_e, $(l_{max}+1)^2$, $d_{attn_value} * N_{heads}$), which is then be reshaped into (n_e, $(l_{max}+1)^2$, N_{heads}, d_{attn_value}). For each edge surrounding the target node, a set of d_{attn_alpha} attention weights are then generated for each attention head, with the total number of heads being N_{heads}. This is used to generate the output vector alpha, which is reshaped along N_{heads} and multiplied with

the reshaped message embedding. Finally, the messages from neighboring are reshaped, rotated back, and aggregated onto the target node, before being projected back into the shape (N_n, $(l_{max}+1)^2$, d_{sphere}).

This is finally passed into a feed-forward network consisting of two linear layers that mixes features of the same l together. The hidden dimensions used in the feed-forward network is given by the hyperparameter d_{ffn}. The edge update block is similar to the node update block, except there is only one convolution layer and no attention required. Between the blocks, layer normalisation is also applied, and similar to EquiformerV2, we also normalised the $l = 0$ features separately from the $l > 0$ features. The final predicted output is passed into the Wigner Eckart layer to be reconstructed into Hamiltonian blocks.

A.1 Wigner Eckart Layer

Our implementation of this layer is similar to that found in Gong et al. (2023). A Hamiltonian block representing the interaction between atom i and j consists can be split into different sub-blocks representing interactions between orbital 1 of order l_1 and orbital 2 of degree l_2 as shown in Fig. 1. Each block of size $(2l_1+1) \times (2l_2+1)$, is an equivariant tensor that comes from the tensor product $l_1 \otimes l_2$ for every pair of interacting orbitals in atom i and atom j. For example, an interaction block between a p orbital ($l = 1$) and a d orbital ($l = 2$) has $(2 \times 1 + 1) \times (2 \times 2 + 1) = 3 \times 5$ elements. We refer to this form as the uncoupled basis representation of the Hamiltonian block.

Before training, the Wigner-Eckart layer converts the Hamiltonian data from uncoupled basis to coupled basis using Clebsch Gordan coefficients.

$l_1 \otimes l_2 = |l_1 - l_2| \oplus ... \oplus (l_1 + l_2)$

$l_1 \otimes l_2$ is now represented by a direct sum of coupled sub-spaces with order ranging from $|l_1 - l_2|$ to $(l_1 + l_2)$. This is repeated for every possible type of orbital interaction between the atoms, to obtain the final direct sum of all the sub-spaces needed for the network to reconstruct the Hamiltonian.

The largest possible $(l_1 + l_2)$ value determines the minimum l_{max} hyperparameter needed for the embeddings of the equivariant model. In the case of HfO_2 in this paper, which uses the SZV basis set, the highest order orbital is the d orbital of Hf. This means that the largest possible (l_1+l_2) comes from the interaction between two Hf d orbitals, and the l_{max} needs to be at least equal to $(2+2) = 4$. This allows the predicted output of the model to be converted back into the full uncoupled basis using the same layer, and reassembled into the full Hamiltonian matrix during inference.

A.2 Loss Computation During Training and Inference

For all experiments, a minor difference from the procedures reported in Yu et al. (2023b) and Schütt et al. (2019) is that we use the Mean Squared Error (MSE) of the full target vectors in the coupled space to compute the fitting and validation loss during training:

$$\mathcal{L}_{MSE}(x_i, \hat{x}_i) = \frac{1}{N}\sum_{i=1}^{N}(x_i - \hat{x}_i)^2$$

Where $\boldsymbol{x}$ and $\hat{\boldsymbol{x}}$ are the flattened targets (orbital blocks). These targets are padded with zeros to ensure that those of different orbital interactions have the same dimensions. To avoid re-shaping the predictions within every epoch, the loss computed during training includes this padding. This is procedure was also used in DeepH E3 (Gong et al. (2023)). However, the final reported loss in Table 6 uses the Mean Absolute Error (MAE) after converting the output and label tensors back into uncoupled space and reconstructing the Hamiltonian blocks.

$$\mathcal{L}_{MAE}(x_i, \hat{x}_i) = \frac{1}{N}\sum_{i=1}^{N}|x_i - \hat{x}_i|$$

The padding is omitted during the reconstruction process, and all the elements in the blocks where the final MAE is computed from represent orbital interactions that exist in the label Hamiltonian.

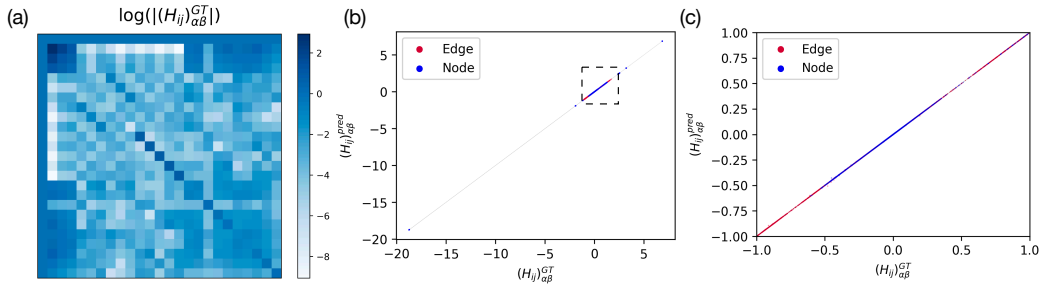

Figure 8: Training the MD17 Hamiltonian matrices of H_2O molecules. (a) Elements of the hamiltonian matrix for a sample H_2O molecule in the dataset. (b) Fitting of the predicted elements of the Hamiltonian matrix against the labels, after randomized downsampling to every 100 data points. Data points closer to the grey line indicate better agreement. (c) Magnification of fit around [-1, 1].

B PERFORMANCE ON SMALL MOLECULES (H_2O)

As our work combines and adapts existing methodology to a new, application-oriented dataset, we first ensure that our adaptation of the networks introduced by Liao et al. (2023) and Wang et al. (2024a) can achieve reasonable results on an existing dataset. We select the dataset of H_2O molecules in MD17 Schütt et al. (2019). The hyperparameters which determine the network size are d_{sphere} and d_{attn_hidden} (**Table 8**). In **Table 5** we explore the effect of these parameters under early-stopping conditions. We fix the number of MP layers to 2 in all cases, lower than was used by similar equivariant GNNs (Unke et al. (2021), Yu et al. (2023b)). Channel dimensions of 32 and above meet the loss defined for the stopping criteria, with larger dimensions reaching it in fewer epochs.

We select a dimension of 64, and train the network under the conditions specified in **Table 8**. In **Table 6** we compare the final Mean Absolute Error (MAE) loss with similar networks in the literature. Our implementation can achieve a prediction accuracy of $\sim$100 meV, which is within an order of magnitude of other equivariant networks while using a smaller network (#MP layers).

Dim.	# Epochs	Training Molecules		Testing Molecules	
		$\epsilon_{\mathbf{node}}$ $[\times 10^{-6} E_h]$	$\epsilon_{\mathbf{edge}}$ $[\times 10^{-6} E_h]$	$\epsilon_{\mathbf{node}}$ $[\times 10^{-3} E_h]$	$\epsilon_{\mathbf{edge}}$ $[\times 10^{-3} E_h]$
16/16	50,000*	0.20*	2.81*	0.1498*	0.4776*
32/32	10,847	0.54	0.43	0.1716	0.1866
64/64	6,761	0.36	0.32	0.1322	0.1534
128/128	2,015*	1.08*	1.01*	0.1878*	0.2776*

Table 5: Effect of the channel dimension used to train the network on H_2O. For this study we remove 1499 molecules from the dataset (4999 total molecules), and use 500 for training (single-batch), 500 for validation, and 499 for testing. For fair comparison between the different network sizes, the trainings were subject to an early-stopping criteria of $\epsilon_{MSE} = 1 \times 10^{-6}$ of the validation set loss. Training losses are reported in MSE while testing losses are reported in MAE. The '*' indicates that the error on the validation set did not reach the stopping criteria, and training instead finished when lr=ϵ_{MSE} (128/128) or when the # epochs reached 50,000.

Network	MAE **H** $[meV]$	MAE **H** $[\times 10^{-6} E_h]$
PhiSNet	0.47	18
QHNet	0.29	11
This work	2.7	100

Table 6: Mean Absolute Error (MAE) for predicted Hamiltonian matrices reported for PhiSNet (Unke et al. (2021)), and QHNet (Yu et al. (2023b)) on the MD17 H_2O dataset, taken from the respective publications. The result for our adapted EquiformerV2 network for electronic property prediction uses 500 molecules for testing, 500 for validation, 2500 for testing. Note that we use 2 layers, as opposed to PhiSNet (4) and QHnet (5).

C AUGMENTING GRAPH PARTITIONS WITH VIRTUAL NODES

Below we detail the procedure to partition the full graph $\mathcal{G}$, described by the set of vertices $\mathcal{V}$ and edges $\mathcal{E}$, into a set of slices $\{\mathcal{G}_1 \ \dots \ \mathcal{G}_N\}$ which are augmented by virtual nodes and edges.

Algorithm 1: Augmented partitioning approach

```
Graph G(V, E) Slice location [x_1 ... x_N] Set of subgraphs {G_1 ... G_N} Numbers labeled
nodes [n_1^n ... n_N^n] Numbers labeled edges [n_1^e ... n_N^e]
for i ← 1 to N do
    V_i ← [];
    n_i^n = 0;
    for v ∈ V do
        if v.x ∈ [x_i, x_{i+1}] then
            V_i.append(v);
            n_i^n += 1;
        end
    end
    E_i ← [];
    n_i^e = 0;
    for v_1 ∈ V_i do
        for v_2 ∈ V_i do
            if v_1 → v_2 ∈ E then
                E_i.append(v_1 → v_2);
                n_i^e += 1;
            end
        end
    end
    for v_1 ∈ V_i do
        for v_2 ∈ V \ V_i do
            if v_2 → v_1 ∈ E then
                V_i.append(v_2);
                E_i.append(v_2 → v_1);
            end
        end
    end
    G_i(V_i, E_i);
end
```

The number of labeled nodes (n_i^n) and the number of labeled edges (n_i^e) are collected and passed to the training functions, which then mask the remainder of the outputs (the virtual nodes and edge outputs) while computing the loss.

D AUGMENTED PARTITION APPROACH WITH TWO MP LAYERS

t_{slice} [Å]	N_t	# Epochs	$\epsilon_{\mathbf{node}}$	$\sigma_{\mathbf{node}}$	$\epsilon_{\mathbf{edge}}$	$\sigma_{\mathbf{edge}}$
∼2	27	16,437	8.24	21.35	0.24	0.39
∼3	28	13,461	8.60	21.01	0.24	0.43
∼4	14	14,089	6.34	15.06	0.24	0.38
∼6	9	11,670	4.46	11.50	0.24	0.39

Table 7: Ablation studies exploring the impact of slice length t_{slice} on the prediction accuracy with 2 MP layers. Values are reported in $\epsilon_n[mE_h]$ and $\sigma_n[\mu E_h]$.

Using 2 MP layers rather than one heavily degrades ϵ_{node} (**Table 3**). This occurs because each slice is augmented with only one layer of virtual connections, so the network does not have a correct

representation of the 2-hop neighborhood. Propagation of this incorrect information into the graph thus results in a degraded ϵ_{node}, which is more sensitive to the extended environment that ϵ_{edge}. The error in this case minimally depends on the outgoing edge (albeit uniformly high). We note that the error with 2 MP layers shows a dependence on t_{slice} (**Table 9**) since larger slices require fewer virtual connections outside the partition.

E HYPERPARAMETERS

We use the hyperparameters shown in Table 8 to train the H_2O benchmark and custom HfO_2 dataset. The ReduceLRonPlaeau scheduler decreases the learning rate by the decay factor when it does not detect a further decrease in validation loss within the decay patience $t_{patience}$. The threshold refers to the sensitivity of the scheduler to changes in validation loss. Once the minimum learning rate is reached, the training stops. The meaning of the hyperparameters are explained in Appendix A. Note that weight decay is not implemented in our study for all cases.

Hyper-parameters	HfO_2/PtGe dataset	MD17 dataset
Optimizer	Adam	Adam
Precision	single (f32)	double (f64)
Scheduler	ReduceLROnPlateau	ReduceLROnPlateau
Initial learning rate	1×10^{-4}	1×10^{-4}
Minimum learning rate	1×10^{-5}	1×10^{-10}
Decay patience $t_{patience}$	500	50
Decay factor	0.5	0.5
Threshold	1×10^{-3}	1×10^{-5}
Interaction distance (Å)	8.0	–
Maximum degree L_{max}	4	4
Maximum order M_{max}	4	4
Number of Message Passing Layers	1	2
Number of spherical channels d_{sphere}	16	64
$f_{ij}^{(L)}$ dimension d_{attn_hidden}	16	64
Number of attention heads N_h	2	2
$f_{ij}^{(0)}$ dimension d_{attn_alpha}	16	32
Value dimension d_{attn_value}	16	32
Hidden dimension in feed forward networks d_{ffn}	64	64

Table 8: Hyper-parameters used for HfO2, PtGe and MD17 data.

E.1 HYPERPARAMETER STUDY

We conducted hyperparameter tuning by training using the full training structure (structure 2), divided into 18 slices of ~ 3 Å thickness. The validation slice used for the scheduler during training was taken from the validation structure, and is centered at the location 26.5 Å. The rest of the hyperparameters follow the values in Table 8. Note that since we are tuning the hyperparameters, we evaluate the trained models with different hyperparameters on the full validation structure (structure 1). The test structure remains unseen throughout this process.

From the table, it is clear that the hyperparameters d_{sphere} , d_{attn_value}, d_{attn_hidden} and d_{attn_alpha} can all be reduced to 16 with little tradeoff in accuracy. Cutting down on the number of parameters allows us to drastically minimise the memory consumption, allowing large graphs to fit into GPU memory during training.

d_{sphere}, d_{attn_hidden}	d_{attn_value}, d_{attn_alpha}	Parameters	Epochs	$\epsilon_{\mathbf{n}}[mE_h]$	$\sigma_{\mathbf{n}}$	$\epsilon_{\mathbf{e}}[mE_h]$	$\sigma_{\mathbf{e}}$
4	32	52,572	31,940	2.82	5.72	0.36	0.84
8	32	125,324	29,002	2.54	5.73	0.18	0.35
16	16	273,644	19,106	2.39	5.31	0.16	0.33
16	32	335,436	16,857	2.46	5.84	0.19	0.35
32	32	1,014,092	14,833	2.51	5.83	0.19	0.37
64	32	3,405,132	11,000	2.47	5.83	0.19	0.37

Table 9: Table of Hyperparameters, tested on the validation structure (structure 1)

F AMORPHOUS HAFNIUM DIOXIDE (A-HfO_2) TRAINING DATA

F.1 DATASET GENERATION

Atomic structures corresponding to materials in the amorphous phase can be produced through melt-quench Urquiza et al. (2021), seed-and-coordinate Youn et al. (2014), or 'decorate and relax' Tafen & Drabold (2003) approaches. To accurately reproduce long-range structural disorder, the structures used must be large enough to avoid the creation of wavefunctions which repeat over periodic boundaries.

The first step to computing the electronic properties of a-HfO_2 is to generate the atomic structure of the material in its amorphous phase. To accurately capture the structural motifs underlying this phase and a realistic range of atomic coordination (eg, neighboring Oxygens for each Hafnium, and vice versa), we start from the crystalline m-HfO_2 phase and perform melt-quench processes using Molecular Dynamics (MD), following a similar procedure as the ones described in Refs. Kaniselvan et al. (2023); Urquiza et al. (2021). We generate 3 independent structures of a-HfO_2 using the QuantumATK toolkit Søren Smidstrup et al. (2020). As the first step, we run an NVT simulation with the Langevin thermostat at 3000 K for 50 ps with a step size of 1 fs. We use the MTP-HfO_2-2022 potential, provided by the software. Next, we run an NPT simulation for 300 ps (and the same 1 fs step size), with an initial reservoir temperature of 3000K and a final temperature of 300K, for a cooling rate of 9K/ps. Finally, we anneal structure evolve at 300K for 50 ps, using the same NVT Langevin thermostat as for the melting.

We then perform a structural relaxation with CP2K code Kühne et al. (2020) to correct for any discrepancies between the relaxed bond lengths attained with the force field used for MD, and those obtained with DFT. Due to the computational cost of using a more complete DZVP basis set VandeVondele & Hutter (2007), we use a simpler SZV basis VandeVondele & Hutter (2007) which uses 4 basis functions per Oxygen atom and 10 basis functions per Hafnium atom. The plane-wave cutoff is set to 500 Ry, while a cutoff of 60 Ry is used for mapping the Gaussian-type orbitals onto the grid. We use the PBE functional for the exchange-correlation energy Perdew et al. (1997). To accurately capture the band gap of a-HfO_2, we applied the Hubbard correction Anisimov et al. (1991) of U = 7 eV to the 3d orbital of Ti and the Hubbard correction of U = 10 eV to the 2p orbital of O.

F.2 ATOMIC BONDING ENVIRONMENTS IN THE AMORPHOUS PHASE

In **Fig. 9** we plot the O-coordination of each Hf atom and the radial distribution function $g(r)$ (where r is inter-atomic distance) for each of the three structures. The distribution in the coordination and dispersion of the peaks in $g(r)$ indicates the amorphous nature of the three structures. Variations between them appear as perturbations in these two quantities. To gain more insights on how different are the structures, we additionally plot the spatially-resolved O-coordination of Hf atoms along the longest, *x* coordinate for the three structures, as well as the distributions of outliers (Hf atoms with very low and very high O-coordination) in three-dimensional space. It is evident that these outliers are situated at different locations in different structures, demonstrating a significant degree of dissimilarity among the structures.

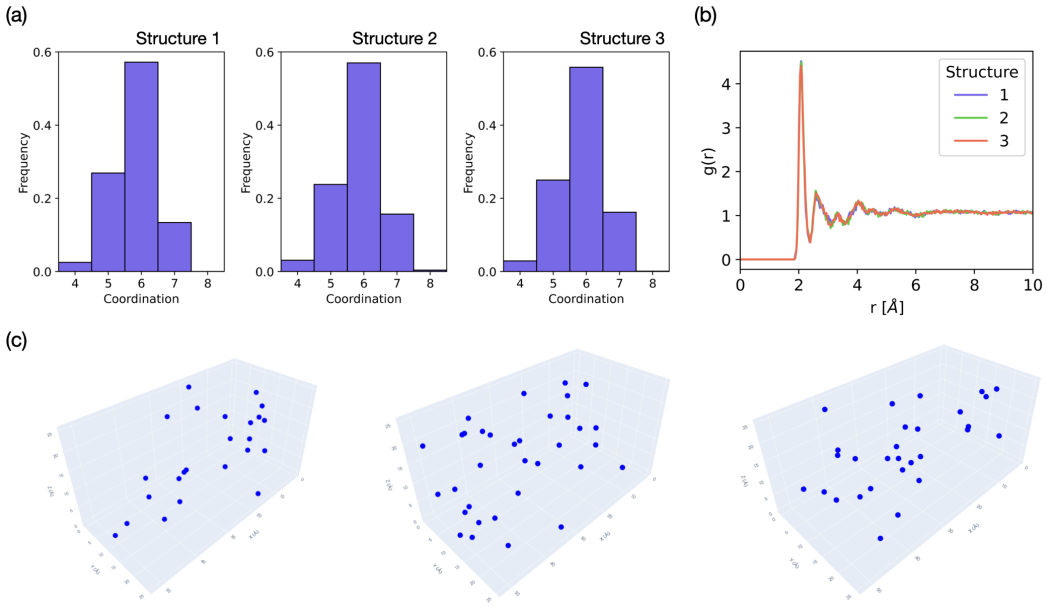

Figure 9: a) O-coordination of Hf atoms (number of O atoms bonding a Hf atom) for each of the generated structures, showing a distribution around a coordination number of 6, and variation between the structures. b) The radial distribution function ($g(r) = \frac{dn(r)}{dr}\frac{V_{domain}}{4\pi r^2 N_{atoms}}$), where $n(r)$ is the number of atoms with distance r between them for the structures 1-3. (c) Spatial distribution of coordination outliers (Hf atoms with O-coordination equal to 8 or 4) for the three structures, which are an indicator of the uniqueness of the three structures.

F.3 Energy eigenvalues

Due to the large cell sizes of the a-HfO_2 structures, all necessary energetic information is contained within the Γ point (where the wavevectors $k_x = k_y = k_z = 0$). The energies at this location can be computed by directly diagonalizing $\mathbf{H}$. Amorphous a-HfO_2 structures corresponding to a realistic distribution of bond lengths should then produce an energy bandgap. We show the distribution of energy eigenvalues for the three structures in **Table 1** in **Fig. 10**, at different values of r_{cut}. In the second row, we zoom into the range of eigenvalues around the energy bandgap, which is defined by the transition between occupied and unoccupied electronic states (the Fermi level $E_F = \sim 0.3E_h$ in all cases). Values of $r_{cut} \geq 8$Å create no noticeable difference on the eigenvalue spectra. Note that the value of $r_{cut} = \infty$ corresponds to the case where no nonzero values were filtered from $\mathbf{H}^{GT}$.

G Compute environment and runtime comparisons

The training is performed with PyTorch Distributed Data Parallel (Li et al. (2020)), where the graph partitions (slices) can be distributed between GPUs.

G.1 Memory consumption of the full graph

During the training of the full graph model, the peak memory consumption observed was 61.68 GiB on a single NVIDIA A100 GPU. Most of the consumption does not stem from the network and the structure but from the additional memory needed for the convolution operations.

G.2 Computational improvement with partitioning approach

In **Fig. 11**, we show the decrease in time per epoch and resulting speedup when using the *augmented partitioning* approach introduced in **Section 3.2**. Since the partitions are independent, the only communication involved in every epoch is a collective to inform each GPU/rank of the loss of each other rank. The time per epoch thus decreases uniformly with the number of slices (N_t) used.

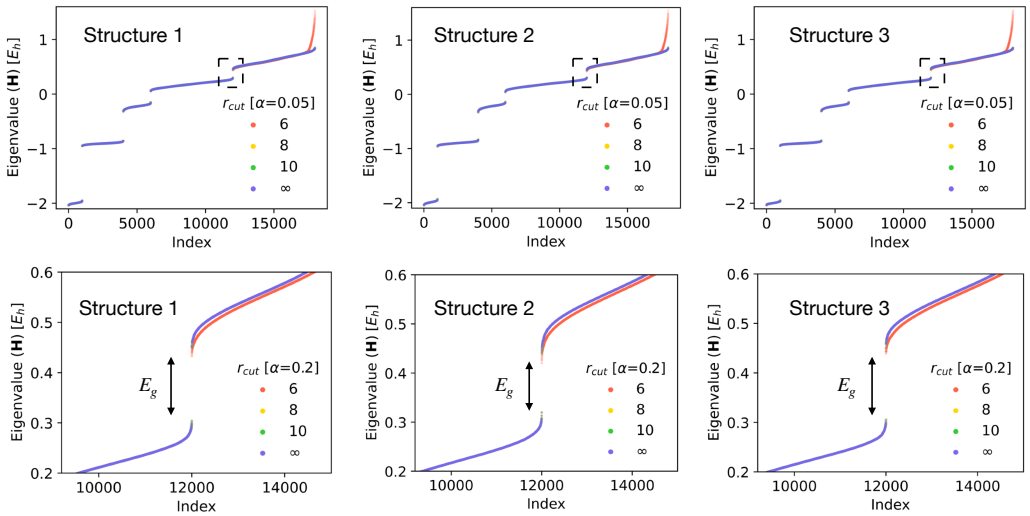

Figure 10: Eigenvalues of the ground-truth Hamiltonian matrix, showing (left) the full eigenvalue spectrum and (right three) zoomed in around the bandgap, for the three structures, in the order of their appearance in **Table 1**.

Despite the independence of each batch and the minimal communication per epoch, the scaling is not perfectly linear. The deviation from an ideal speedup can be attributed to two factors:

- Load imbalance: The partitioning approach was designed to leverage the periodicity in the y- and z- direction within a straightforward implementation. However, it is not ideal in terms of the number of cuts/number of virtual nodes/edges required, resulting in a slightly different amount of work per rank which leads to an observable load imbalance at higher N_t. This effect can be seen in the allocated memory per partition (**Fig. 11(c)**). We note that the *augmented partitioning* method can be used with any standard graph-partitioning algorithm.

- Computational overhead of the virtual nodes and edges: Individual nodes and edges of the graph can be repeated in labeled and virtual node lists. Treating the replicas introduces additional computational cost while training the network, which increases with N_t. This overhead is maximum with the use of very small slices (large N_t), thus introducing a trade-off between parallelism and time per epoch.

G.3 H_2O vs HfO_2 runtimes

In **Section 4.4**, we make a comparison between the computational cost of computing the Hamiltonian for an H_2O molecule and the HfO_2 structure. However, the Hamiltonians for the H_2O molecules in the MD17 dataset were computed by Schütt et al. (2019) using different compute infrastructure. To approximate the cost of generating such a dataset under the same computational conditions, we set up CP2K simulations with a Double-ζ Valence Polarized (DZVP) basis, which includes a similar set of valence and polarization functions as the def2_SVP basis used with the ORCA code (Neese (2011)) to generate the H_2O Hamiltonians for the MD17 dataset. A minor difference is that the def2_SVP basis includes an extra s-type orbital on Oxygen (14 total per Oxygen atom). Under these conditions, the computation time per H_2O molecule was 7s, when run on 12 nodes with 12-core Intel Xeon E5-2680 CPUs and NVIDIA P100 GPU (the Piz Daint supercomputer), resulting in a total of 0.04 node hours. The HfO_2 structures requires 3.65 node hours in the same compute environment (but distributed to 27 nodes). The difference, omitting scaling behavior, is roughly $\sim$100$\times$.

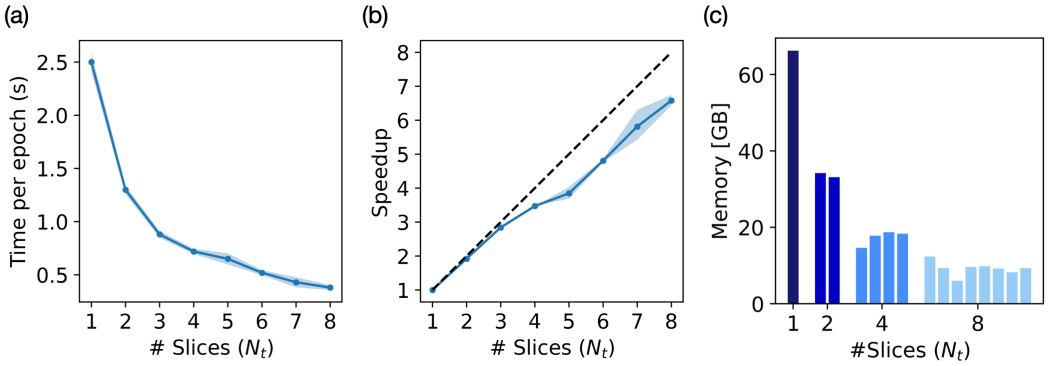

Figure 11: (a) Time per epoch and (b) speedup resulting from the use of increasing numbers of slices N_t. Median values are shown, while the error bands are one standard deviation. Experiments were run on NVIDIA A100 GPUs with # ranks set to N_t. Measurements are only shown up to 8 slices/8 GPUs due to limitations in available compute resources at the time of submission. The fill-between indicates the range in runtime over the first 30 minutes of training. The dashed black line corresponds to the ideal speedup, in which case the use of N_t slices would enable an $N_t\times$ speedup in the runtime per epoch. (c) Measured peak memory consumption as a function of the number of partitions, where each bar corresponds to a different GPU. Variation in memory consumption between GPUs at each individual value of N_t translate to load imbalance, which correlates with the deviation from ideal scaling shown in (b).

H Comparisons between DFT and Predicted Hamiltonians

In **Figure 12**, we plot the MAE error as a function of different interactions between the orbital basis of the a-HfO_2 test structure. The data is plotted in log scale to magnify the asymmetry resulting from the separate training of the two-way edges between labeled nodes in the graph.

In **Fig. 13**, we plot the comparison between $\boldsymbol{H}^{pred}$ and $\boldsymbol{H}^{GT}$ (as shown in the main text) for three separate cases: (1) using the upper triangle, (2) the lower triangle, and (3) the symmetrized $\boldsymbol{H}^{pred}$. We also zoom in around the bandgap in the second row. In all three cases, $\boldsymbol{H}^{pred}$ is unchanged, indicating that the small asymmetry in the matrices caused by the existence of separate forward/backward edges between atoms has a minimal effect. In the third row, we show the error in log scale as a function of the eigenvalue index, sorted in the same order as shown in the first row. The error is largest around the band edges, where orbital coupling is most significant.

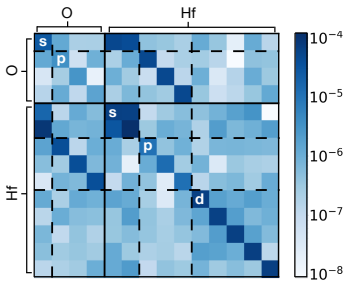

Figure 12: Average ϵ_{MAE} between $(H_{ij})^{GT}$ and $(H_{ij})^{pred}$ for specific inter-atomic orbital coupling. The data is shown in log scale to magnify asymmetry in the error.

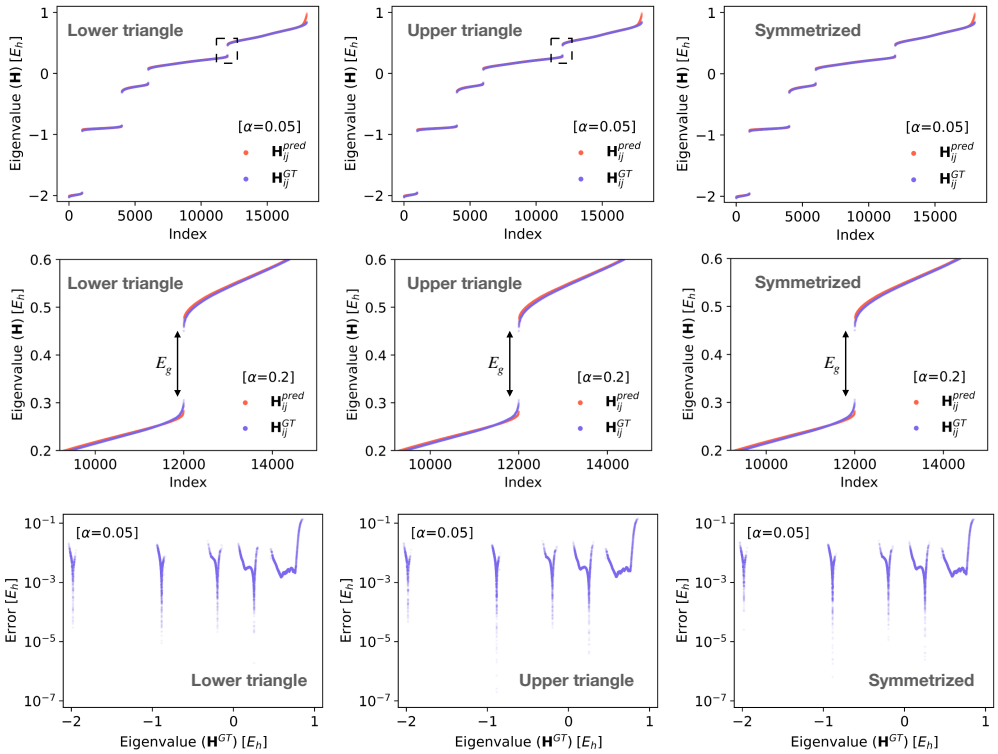

Figure 13: Comparison between $\boldsymbol{H}^{GT}$ and $\boldsymbol{H}^{pred}$, using the upper/lower triangle or symmeterized version of $\boldsymbol{H}^{pred}$. The center row shows the same plots zoomed in around the bandgap. The last row shows the difference in the eigenvalue spectra. The structures appear in the order of **Table 1**.

Structures Training	Structures Testing	Epochs	$\epsilon_{\mathbf{n}}\,[mE_h]$	$\sigma_{\mathbf{n}}\,[\mu E_h]$	$\epsilon_{\mathbf{e}}\,[mE_h]$	$\sigma_{\mathbf{e}}\,[\mu E_h]$	$\epsilon_{\mathbf{tot}}\,[mE_h]$	$\epsilon_{\mathbf{tot}}\,[meV]$
0	3	15675	2.29	5.09	0.20	0.38	0.22	5.87
0, 2	3	48356	2.22	4.99	0.12	0.25	0.13	3.55

Table 10: Comparison of models trained on one HfO_2 structure (structure 2) vs two HfO_2 structures (0 and 2). Both are tested on a fully unseen structure (3), showing improved accuracy from 5.87 to 3.55 meV.

Oxygen vacancies Training set	Oxygen vacancies Testing set	$\epsilon_{\mathbf{n}}\,[mE_h]$	$\sigma_{\mathbf{n}}\,[\mu E_h]$	$\epsilon_{\mathbf{e}}\,[mE_h]$	$\sigma_{\mathbf{e}}\,[\mu E_h]$
5%	5%	2.44	5.06	0.16	0.31
5%	10%	2.58	5.23	0.18	0.33
5%	15%	2.50	4.96	0.17	0.33
10%	5%	2.48	5.12	0.18	0.33
10%	10%	2.50	4.96	0.17	0.33
10%	15%	2.60	4.89	0.18	0.33
15%	5%	2.94	6.45	0.16	0.34
15%	10%	2.52	5.01	0.16	0.34
15%	15%	2.52	4.69	0.16	0.31

Table 11: HfO_2 models trained and tested with different stoichiometry using augmented partitioning. 18 slices of each structure, each 3 Å thick, was used for training. The training method is identical to the one used to obtain Table 4. Models trained on vacancies 5%, 10 % and 15% vacancies are tested on test structures with vacancies ranging from 5% to 15%.

I Additional Tests

I.1 Using Two HfO_2 Structures for Training

While training on a single structure is sufficient to achieve the results in **Fig. 6**, increasing the quantity of training data further leads to improved prediction accuracy. To demonstrate this, we train using *augmented partitioning* on two structures, including structure 2 from **Table 1** as well as a newly generated structure "0" of similar size (3000 atoms). Training was performed with 18 slices of 3 Å thickness taken from both structures, validated on structure 1, and tested on structure 3. The results are compared against the previous model trained on one structure in Table 10, showing that the prediction accuracy can be improved from 5.87 meV to 3.55 meV by using 2$\times$ the number of slices for training.

I.2 Sub-stoichiometric Hafnium Oxide

Amorphous HfO_2 often exists in a sub-stoichiometric form (HfO_x), which can be interpreted as the presence of oxygen vacancies. In this section we evaluate whether our model can extend to train and predict such defective structures.

To do this, we create a dataset for sub-stoichiometric HfO_x structures by introducing randomly distributed oxygen vacancies into the original, pristine HfO_2 structures. The sub-stoichiometric structures are generated for x = 1.9, 1.8, and 1.7 (corresponding to vacancy concentrations of 5%, 10%, and 15 %, respectively). Vacancies are treated as ghost atoms (atoms with no orbitals, but with a basis set defined at their locations), to mitigate the basis set superposition error Senent & Wilson (2001), a known problem related to localized basis sets. More precisely, by treating vacancies as ghost atoms, one prevents the excessive borrowing of the basis sets from neighboring atoms by the vacancy, which improves the accuracy of the predicted electronic properties. These ghost atoms are assigned an atomic number of 0. The training and testing approach is similar to the one used to obtain Table 4, except that now oxygen vacancies are considered. For all experiments, 18 slices (3 Åthick) were used.

The results are summarized in Table 11. The ϵ_n and ϵ_e values across different experiments lie within a small range (2.50-2.90 mE_h and 0.16-10.18 mE_h respectively), showing that the network generalizes well to structures of different vacancies, regardless of which vacancy configuration it was

Training method method	**Oxygen vacancies Testing set**	$\epsilon_\mathbf{n}\,[mE_h]$	$\sigma_\mathbf{n}\,[\mu E_h]$	$\epsilon_\mathbf{e}\,[mE_h]$	$\sigma_\mathbf{e}\,[\mu E_h]$
partitioned	5%	2.94	6.45	0.16	0.34
partitioned	10%	2.52	5.01	0.16	0.34
partitioned	15%	2.52	4.69	0.16	0.31
full	5%	2.96	6.07	0.19	0.38
full	10%	2.67	5.18	0.18	0.36
full	15%	2.64	4.83	0.17	0.35

Table 12: Comparison between full graph training and the augmented partitioning training using the same HfO_2 structure with 15% vacancies. Models are tested on structures with vacancies ranging from 5% to 15%.

Material	**Cutoff** $[\AA]$	$\epsilon_\mathbf{n}\,[mE_h]$	$\sigma_\mathbf{n}\,[\mu E_h]$	$\epsilon_\mathbf{e}\,[mE_h]$	$\sigma_\mathbf{e}\,[\mu E_h]$	$\epsilon_\mathbf{tot}\,[mE_h]$	$\epsilon_\mathbf{tot}\,[meV]$
Crystalline HfO_2	8	0.01	0.02	0.04	0.07	0.04	1.17
Amorphous HfO_2	8	2.29	5.09	0.20	0.36	0.22	5.87
Amorphous PtGe	16	0.87	1.43	0.05	0.10	0.05	1.43

Table 13: Summary of models trained on crystalline HfO_2, amorphous HfO_2 and amorphous PtGe materials, respectively. The HfO_2 model was trained on different slices of the same crystalline structures. On the other hand, the PtGe model was trained on a single 5 Å slice of structure 1 and tested on on a fully unseen structure 2.

trained on. To demonstrate that the *augmented partitioning* approach similarly does not affect accuracy for sub-stoichiometric HfO_x, we also perform full graph training using structure 2 with 15% vacancies, and compare with the *augmented partitioning* approach in Table 12. The minimal difference in ϵ_n and ϵ_e values between full and partitioned approaches indicates that both approaches generalize equally well to different stoichiometry. These values are also close to that of stoichiometric HfO_2 in Table 4, demonstrating that the augmented partitioning approach can also be applied even in the case of more realistic sub-stoichiometric structures.

I.3 Crystalline Hafnium Oxide

Crystalline materials contain highly regular atomic environments, and are thus a natural extension of this approach. Although such a large unit cell is not required for a crystal, we nevertheless generate a single crystalline HfO_2 structure (in its monoclinic phase) containing 3000 atoms for comparison. The model was trained on a single slice taken from x = 0 Å, validated on a slice from x = 15 Å, and tested on an unseen slice from x = 20 Å. Results in Table 13 show that a high accuracy close to sub-meV can be achieved.

I.4 Second Material Example: PtGe

Finally, we test if the model and training approach can be used for different material systems. We consider the example of two amorphous PtGe structures, labelled 1 and 2, each containing 2688 atoms. These structures were similarly generated in CP2K. A larger cutoff radius of 16 Å was chosen due to the larger spacing between atoms. The model was trained on a single 5 Å slice taken from x = 10 Å and validated on another slice at x = 20 Å, both from structure 1. The trained model was then tested on a full unseen structure (structure 2), with results shown in Table 13. The final obtained error for all 2688 atoms and 2,148,055 edges is 1.43 meV, much lower than that of HfO_2, despite the lower amount of training data. This demonstrates the generalizability and robustness of

Cutoff $[\AA]$	$\epsilon_\mathbf{n}\,[mE_h]$	$\sigma_\mathbf{n}\,[\mu E_h]$	$\epsilon_\mathbf{e}\,[mE_h]$	$\sigma_\mathbf{e}\,[\mu E_h]$	$\epsilon_\mathbf{tot}\,[mE_h]$	$\epsilon_\mathbf{tot}\,[meV]$
6	0.87	1.43	0.15	0.19	0.17	4.60
8	0.87	1.42	0.09	0.16	0.10	2.73
16	0.87	1.43	0.05	0.10	0.05	1.43

Table 14: Prediction accuracy of model on amorphous PtGe material with different r_{cut}

the augmented partitioning approach when applied to different material dataset with a much larger cutoff radius.

We perform a similar study on the cutoff radius and connectivity of the PtGe, through both eigenvalue analysis and the convergence study of cutoff-radii, with results shown in Table 14 and Figure 14. Increasing the cutoff radius once again increases the overall prediction accuracy of the trained model, with the improvement especially noticeable at the edges.

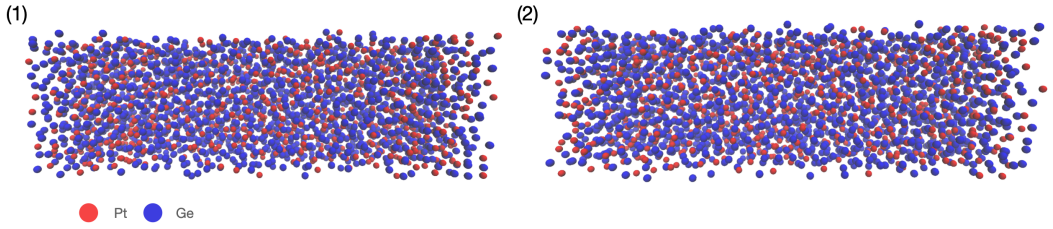

Figure 14: Atomic coordinates of the two amorphous PtGe structures.